Master's Theses

Graduate College

12-2005

# A K-Epsilon Extension for Wall-Bounded Flows on the Broadband Aeroacoustic System Simulator

David González

## Recommended Citation

González, David, "A K-Epsilon Extension for Wall-Bounded Flows on the Broadband Aeroacoustic System Simulator" (2005). *Master's Theses*. 4235.
https://scholarworks.wmich.edu/masters_theses/4235

A K-EPSILON EXTENSION FOR WALL-BOUNDED FLOWS ON THE
BROADBAND AEROACOUSTIC SYSTEM SIMULATOR

by

David González

A Thesis
Submitted to the
Faculty of The Graduate College
in partial fulfillment of the
requirements for the
Degree of Master of Science in Engineering (Mechanical)
Department of Mechanical and Aeronautical Engineering

Western Michigan University
Kalamazoo, Michigan
December 2005

## ACKNOWLEDGEMENTS

# A K-EPSILON EXTENSION FOR WALL-BOUNDED FLOWS ON THE BROADBAND AEROACOUSTIC SYSTEM SIMULATOR

David González, M.S.E.

Western Michigan University, 2005

The turbulence modeling capabilities of the Broadband Aeroacoustic System Simulator (BASS), an experimental code developed at NASA Glenn Research Center, have been extended to include wall-bounded flow capabilities. This was done by first validating the code's viscous solving routines by comparing numerical solutions to known, simple analytical solutions. Finally, the dynamics of the wall shear flows were accounted for with the use of wall-damping functions incorporated into the turbulence model. The results for both the viscous and turbulence routines agree well with published data.

# TABLE OF CONTENTS

Table of Contents-Continued

# LIST OF TABLES

# LIST OF FIGURES

# CHAPTER I

# INTRODUCTION

For the past twenty years, computational fluid dynamics (CFD) has continually grown to become one of the more indispensable tools for engineers today. With the continuing growth of computer processing capabilities it is becoming possible to model flow situations which have previously been impossible. The ultimate goal is to be able to accurately compute turbulent flows in complex geometries in a minimal amount of time. However, due to the nature of turbulent flows, some speculate that we are still quite a few years away from being to directly model most flows of interest.

## Introduction to Turbulence

The reasons for being so far from having the capabilities to simulate turbulence directly are embedded in its nature. There is no set definition of turbulence but, after Hinze (1975), "Turbulent fluid motion is an irregular condition of flow in which the various quantities show a random variation with time and space coordinates so that statistical average values can be discerned." The general consensus, going along with Hinze's description, is that a turbulent flow displays the following characteristics (Tennekes and Lumley 1972):

- randomness;

- diffusivity;

- high Reynolds numbers;

- three-dimensional vorticity fluctuations;

- dissipation; etc.

Everybody is familiar with the randomness associated with turbulent flows. It is evident in cigarette smoke (Figure 1) where a laminar stream quickly degrades into a chaotic flow. This randomness eliminates any possibility of performing any kind of direct deterministic analysis. Instead, analysis relies on statistical approaches.
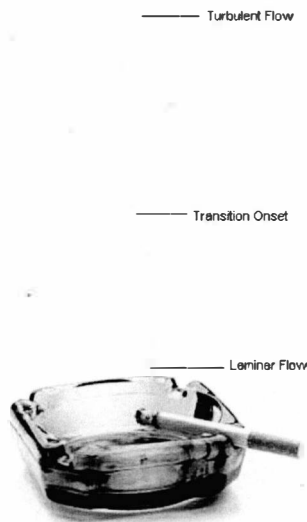


Figure 1. Degradation of Laminar Flow to Turbulent.

The diffusive character of turbulence is perhaps the one characteristic that engineers are more interested in one. Increased rates of momentum, heat, and mass transfers are the direct result of diffusion. Because of this, some applications may find the presence of a turbulent flow as desirable (heat transfer in a heat exchanger) while others try to avoid them as much as possible (flow in pipelines).

A Reynolds number ($Re$) can be interpreted as the ratio of viscous to inertial forces in a fluid. Turbulence is always encountered at large Reynolds numbers. It usually originates from some kind of disturbance or instability that develops from a laminar flow. These disturbances, in turn, are caused by the interaction between the viscous and nonlinear inertia terms in the governing equations.

Dissipation and three-dimensional vorticity fluctuations are also important in distinguishing a turbulent flow from one that is just random. The vorticity, and hence the flow, needs to be three-dimensional because the phenomenon known as vortex stretching, which maintains the vorticity and turbulence, is only present in three-dimensional flows.

Flows which are turbulent also exhibit a vast range in length scales. The structures known as eddies are responsible for the fluctuations in the flow properties and can be as small as a few times the mean free path ($\lambda$) or as large as any transverse scale like, for example, the diameter of a pipe. All of these scales play an integral part in the description of the turbulent flow.

It is believed that the unsteady Navier-Stokes equations provide adequate descriptions of all of these phenomena. Since even the smallest of eddies are larger than the mean free path, turbulence is considered a continuum phenomenon (Chen *et al.* 1998). For compressible flows, the Navier-Stokes equations (NSEs) are:

Conservation of mass

$$\rho_{,t} + \left( \rho u_i \right)_{,i} = 0 \tag{1.1}$$

Conservation of momentum

$$\left( \rho u_i \right)_{,t} + \left( \rho u_j u_i \right)_{,j} = \sigma_{ij,j} \tag{1.2}$$

Conservation of energy

$$(\rho E)_{,t} + (\rho E u_i)_{,i} = (\sigma_{ij} u_j)_{,i} - q_{i,i} \qquad (1.3)$$

Equation of state

$$p = \rho R T \qquad (1.4)$$

where,

$$E = e + \frac{1}{2} u_i u_i, \qquad e = C_v T, \qquad \sigma_{ij} = -p\delta_{ij} + \tau_{ij}$$

$$\tau_{ij} = \mu(u_{i,j} + u_{j,i}) - \frac{2}{3}\mu u_{k,k}\delta_{ij}, \qquad q_i = -kT_{,i}$$

and $(\ )_{,t}, (\ )_{,i}$ stand for derivatives with respect to $t$ and $x_i$, respectively.

However, even having a system of equations capable of describing the phenomenon does not solve the problem. The NSEs are a collection of highly nonlinear partial differential equations to which there is not closed-form solution. To add to this predicament, in order to describe turbulence to the fullest additional parameters need to be derived from the NSEs and the procedure results in further increasing the nonlinearity of the equations.

As mentioned earlier, the computational effort to resolve every scale and moment in the flow accurately is just too great. To illustrate the magnitude of the numerical and computational complexity, Wilcox (1998) estimated the number of grid points necessary to directly simulate turbulence by the following expression:

$$N_{DNS} = (0.088\,\mathrm{Re}_h)^{9/4} \qquad (1.5)$$

So with a $Re$ of 7000, a total of around 2 million grid points are necessary to run the simulation.

# Turbulence Modeling

As evidenced by the above discussion, the direct numerical simulation (*DNS*) of turbulence is not a viable solution for engineers since typical engineering flows are at Reynolds numbers of the order of $10^5$ or greater. The question to ask is: What can be done to simplify the simulation of turbulent flows? The answer lies in turbulence modeling and depends greatly on the application as well as the engineer's needs.

Turbulence modeling can be divided into three parts:

- direct numerical simulation (DNS);

- large-eddy simulation (LES); and

- averaged equations.

DNS has already been described briefly. Two very common averaging techniques can be applied to the Navier-Stokes equations to analyze turbulence. They are the Reynolds (RANS) and Favre averages and both entail decomposing the flow properties into mean and fluctuating parts. This procedure has the negative effect of ignoring the fine details of the turbulence structure.

For the most part, the engineer is not necessarily interested in knowing the dynamics and contribution of every single length scale in the flow. He is more interested in how the energy-bearing large eddies develop and what they contribute to the mean flow. That is why the RANS equations have such widespread use in industry; it offers enough detail to the engineer without requiring relatively large computational effort.

## Large-Eddy Simulation

A procedure that holds much promise is large-eddy simulation (*LES*). Whereas RANS models every scale in the flow, in LES, only the smaller scales are modeled while the larger are computed directly. Again, the larger scales are of interest because they are the ones that actually control turbulent diffusion (Lesieur *et al.* 1996). Instead of performing an average to isolate the large scales, LES makes use of filters.

This filtering, as well as the averaging in RANS and the development of closure equations for DNS, introduces extra moments into the governing equations which results in there being more unknowns than equations. This is the closure problem and can be illustrated by considering the Navier-Stokes equations in incompressible form:

$$\left(u_i\right)_{,t} + \left(u_i u_j\right)_{,j} = -\frac{1}{\rho_0}p_{,j} + \left[\nu\left(u_{i,j} + u_{j,i}\right)\right] \tag{1.6}$$

Lesieur *et al.* (1996) applied the following filter to the above equations,

$$\bar{f}(\mathbf{x},t) = \int f(\mathbf{y},t)\overline{G}(\mathbf{x}-\mathbf{y})d\mathbf{y} = \int f(\mathbf{x}-\mathbf{y},t)\overline{G}(\mathbf{y})d\mathbf{y} \tag{1.7}$$

obtaining

$$\left(\bar{u}_i\right)_{,t} + \left(\bar{u}_i\bar{u}_j\right)_{,j} = -\frac{1}{\rho_0}\bar{p}_{,i} + \left[\nu\left(\bar{u}_{i,j} + \bar{u}_{j,i}\right) + T_{ij}\right] \tag{1.8}$$

Comparing equations (1.6) and (1.8), an additional term was obtained as a result of the filtering. This term is the subgrid-scale tensor and is given by $T_{ij} = \bar{u}_i\bar{u}_j - \overline{u_i u_j}$. This tensor is the additional moment introduced and some type of hypothesis needs to be made in order to close the system of equations.

The most common hypothesis is the Boussinesq approximation and it suggests that the turbulent shearing stresses may be related to the rate of mean strain through a

scalar value termed the turbulent (eddy) viscosity, $v_T$. For the subgrid-scale tensor of

equation 1.8, the approximation based on Boussinesq's hypothesis is:

$$T_{ij} = 2v_t \overline{S}_{ij} + \frac{1}{3} T_{ll} \delta_{ij} \qquad (1.9)$$

where,

$$\overline{S}_{ij} = \frac{1}{2} \left( \overline{u}_{i,j} + \overline{u}_{j,i} \right) \qquad (1.10)$$

In the end, the LES equations are simplified marginally since a new term, $v_T$, is added

and still needs to be modeled. However, the more difficult approximations have already

been made.

Many models have been used to close the turbulent eddy viscosity. Smagorinsky

(1963) used a mixing-length-type model in which he assumed the eddy viscosity to be

proportional to the subgrid-scale characteristic length, $\Delta x$, and to a characteristic

velocity. Other based their approximations on more complicated assumptions, for

example, Kraichnan (1976) used the kinetic-energy spectrum as a basis for his

approximation.

## Two-Equation Turbulence Model

Like Smagorinsky, the work here centered on computing the turbulent viscosity

from a parameter describing a characteristic length and another describing a characteristic

velocity. However, whereas he obtained the relevant scales from the local flow

parameters, a two-equation turbulence model in which two additional partial-differential

equations are solved along with the flow to determine these scales was used. Solving

these equations accounts for the upstream history of the flow (Tannehill *et al.* 1997).

The turbulent kinetic energy, $k = \frac{1}{2} u_i' u_i'$, is usually used to obtain the velocity scale by setting it equal to the square root of $k$. Others have developed models that solve for the square root of $k$ directly, *ie* $q = \sqrt{k}$ (Coakley 1983).

For the length scale, there have also been several suggestions as to an appropriate quantity that describes its evolution. Some have developed equations to solve for $l$ directly but have found that parameter to be ill-conditioned as a dependent variable. There are two other parameters that are widely used for the second equation; the vorticity (Wilcox 1998), $\omega$, and the dissipation rate of turbulent kinetic energy, $\varepsilon$. Of the two, the dissipation rate has received the most attention largely due to the work of Harlow and Nakayama (1968), which were responsible for developing the so-called "standard" $k$-$\varepsilon$, and Jones and Launder (1972), who were the first to extend the standard model to allow the resolution of low Reynolds number turbulent flow.

The two-equation model used in this project is a variation of the $k$-$\varepsilon$ model. The transport partial differential equations for these parameters can be developed from the Navier-Stokes equations (1.1-1.4). The turbulent kinetic energy ($k$) is obtained by multiplying equation (1.2) for the $i^{th}$ variable by $u_j$, multiplying (1.2) for the $j^{th}$ variable by $u_i$ and adding both. After the results are added, we simply set $i=j$. For the dissipation rate, equation (1.2) for the $i^{th}$ variable should be differentiated with respect to $x_j$ and multiplied afterwards by $2\mu \dfrac{\partial u_i}{\partial x_j}$.

These two equations are quite complex and not of particular use in their crude form (see, for example, Shih *et al.* 1995). Therefore, further refinement is necessary. Since there are so many additional moments created by manipulating the Navier-Stokes

8

equations by the procedures outlined above, one seeks to determine which of the moments contribute to the important processes in turbulence, namely diffusion, production and dissipation, and modeling each process individually. This greatly reduces the number of terms in the equation.

After this is done, the following are the additional transport equations solved in the standard $k$-$\varepsilon$ model:

Turbulent Kinetic Energy:

$$
\begin{aligned}
\left(\overline{\rho}\widetilde{k}\right)_{,t} + \left(\overline{\rho}\widetilde{u}_j\widetilde{k}\right)_{,j} &= \left[\left(\mu + \mu_T\big/\mathrm{Pr}_k\right)\widetilde{k}_{,k}\right]_{,j} \\
&+ \left[2\mu_T\left(S_{ij} - \frac{1}{3}\delta_{ij}\widetilde{u}_{k,k}\right) - \frac{2}{3}\overline{\rho}\widetilde{k}\delta_{ij}\right]\widetilde{u}_{i,j} - \overline{\rho}\widetilde{\varepsilon}
\end{aligned}
\tag{1.11}
$$

Dissipation of Turbulent Kinetic Energy:

$$
\begin{aligned}
\left(\overline{\rho}\widetilde{\varepsilon}\right)_{,t} + \left(\overline{\rho}\widetilde{u}_j\widetilde{\varepsilon}\right)_{,j} &= \left[\left(\mu + \mu_T\big/\mathrm{Pr}_k\right)\widetilde{\varepsilon}_{,j}\right] \\
&+ C_{\varepsilon1}\frac{\widetilde{\varepsilon}}{\widetilde{k}}\left[2\mu_T\left(S_{ij} - \frac{1}{3}\delta_{ij}\widetilde{u}_{k,k}\right) - \frac{2}{3}\overline{\rho}\widetilde{k}\delta_{ij}\right]\widetilde{u}_{i,j} - C_{\varepsilon2}\overline{\rho}\frac{\widetilde{\varepsilon}^2}{\widetilde{k}}
\end{aligned}
\tag{1.12}
$$

with $\mu_T$ given by $\mu_T = C_\mu \overline{\rho}\dfrac{\widetilde{k}^2}{\widetilde{\varepsilon}}$. In these equations, the terms $C_\mu$, $C_{\varepsilon1}$, and $C_{\varepsilon2}$ are model coefficients determined experimentally. The terms on the right-hand side of both equations represent left-to-right, the diffusion, production, and dissipation rates of $k$ and $\varepsilon$, respectively.

This turbulence model is not without its faults. Among them is the fact that two-equation models, in general, have the problem of not being able to accurately predict separation in adverse pressure gradient flows (Menter 1994). Also, Shih *et al.* (1995) point out that the standard dissipation rate equation may not always provide the

appropriate length scales, so alternative formulations may have to be employed. Perhaps the biggest concern with the above model is that it is formulated for high Reynolds number flows and results in the model not being able to predict viscous interactions in the low Reynolds number regions created by the presence of a wall (Jones and Launder 1973).

## BASS Code

The numerical platform for this project is NASA's Broadband Aeroacoustic System Simulator (BASS) code. It is a large-eddy simulation code developed to analyze the complex interactions between sound and structures. As its name reflects, it is a computational aeroacoustics (CAA) code. While CAA and CFD share many things in common, they are two separate fields and each is concerned with a totally different result. The following is a brief comparison between the two fields.

The main objective behind CAA is to predict the pressure fluctuations responsible for the generation of sound and their propagation (Hixon *et al.* 1995 and Tam 1995). This means that CAA relies on time-dependent solutions of the governing equations. CFD's goal, on the other hand, is to resolve the *time-independent* mean flow to predict steady-state aerodynamic forces.

This difference brings about several issues that are unique to aeroacoustics. The first is that sound is broadband, *ie* it incurs a wide frequency spectrum, much like the range in length scales encountered in turbulent flows. In order to resolve these frequencies, it is customary to have around 6 to 8 mesh points per wavelength (Tam 1995). The domain will therefore require a great amount of grid points for the accurate

prediction of sound propagation and the development of finite difference algorithms that are both accurate and fast is really important.

Since the computational domain will always be finite, there is a need to develop unsteady boundary conditions that minimize reflections of the pressure waves as they exit the domain. Different types of analyses have been performed to develop these boundary conditions. Tam and Webb (1993) performed an asymptotic analysis on the Euler equations with constant mean flow to develop radiation boundary conditions; Thompson (1987 and 1990) and Giles (1990) based their boundary conditions on characteristic theory, while still others looked at absorbing boundary conditions. A thorough comparison of the performance of these boundary conditions can be found in Hixon *et al.* (1995) and Hixon *et al.* (2000).

These and other aspects of the aeroacoustics science make CAA considerably more complex than CFD. However, with all of their complexity, CAA codes can be used for to acquire steady-solutions. After all, both sciences make use of the same equations.

The BASS code, hence, is designed to solve two- and three-dimensional unsteady nonlinear flows in complex geometry domains. It does this by marching the governing equations in time in generalized coordinates. The code is robust in the sense that it allows the user to solve either the Euler or full Navier-Stokes equations. These can be written is Cartesian coordinates as:

$$\frac{\partial Q}{\partial t} = -\left( \frac{\partial E}{\partial x} + \frac{\partial F}{\partial y} + \frac{\partial G}{\partial z} \right) \tag{1.13}$$

Equation (1.13) has already been rewritten to its time-marching form.

BASS performs its computations with nondimensional variables. The corresponding nondimensionalizing parameters are highlighted in Table 1. The reference length ($L_{ref}$) below is arbitrarily input by the user. For simplicity, it is chosen to be *1.0 m*, essentially leaving the magnitude of the dimensional and nondimensional grid variables the same. The velocities are nondimensionalized by the speed of sound ($a$) at standard atmosphere conditions, while $T_{ref}$ is the total temperature at the same conditions.

The nondimensional Navier-Stokes (NDNSE) equations become:

$$Q = \begin{bmatrix} \rho^* \\ \rho^* u^* \\ \rho^* v^* \\ \rho^* w^* \\ E_t^* \end{bmatrix}, E = \begin{bmatrix} \rho^* u^* \\ \rho^* u^{*2} + p^* - \tau_{xx}^* \\ \rho^* u^* v^* - \tau_{xy}^* \\ \rho^* u^* w^* - \tau_{xz}^* \\ \left(E_t^* + p^*\right)u^* - u^* \tau_{xx}^* - v^* \tau_{xy}^* - w^* \tau_{xz}^* + q_x^* \end{bmatrix},$$

$$F = \begin{bmatrix} \rho^* v^* \\ \rho^* u^* v^* - \tau_{xy}^* \\ \rho^* v^{*2} p^* - \tau_{yy}^* \\ \rho^* v^* w^* - \tau_{yz}^* \\ \left(E_t^* + p^*\right)v^* - u^* \tau_{xy}^* - v^* \tau_{yy}^* - w^* \tau_{yz}^* + q_y^* \end{bmatrix},$$

(1.14)

$$G = \begin{bmatrix} \rho^* w^* \\ \rho^* u^* w^* - \tau_{xz}^* \\ \rho^* v^* w^* - \tau_{yz}^* \\ \rho^* w^{*2} + p^* - \tau_{zz}^* \\ \left(E_t^* + p^*\right)w^* - u^* \tau_{xz}^* - v^* \tau_{yz}^* - w^* \tau_{zz}^* + q_z^* \end{bmatrix}$$

where $E_t^* = \rho^*\left(e^* + \dfrac{u^{*2} + v^{*2} + w^{*2}}{2}\right)$, $q_i^* = -\dfrac{\mu^*}{(\gamma - 1)\mathrm{Re}_{ref}\,\mathrm{Pr}}T_{,i}^*$. Note that the turbulent

variables, $k$ and $\varepsilon$, still have not been accounted for in the above equations.

| Variable | Nondimensionalizing Parameter |
| --- | --- |
| $X$ | $L_{ref}$ |
| $Y$ | $L_{ref}$ |
| $Z$ | $L_{ref}$ |
| $U$ | $a$ |
| $V$ | $a$ |
| $W$ | $a$ |
| $\mu$ | $\mu_{ref}$ |
| $\rho$ | $\rho_{ref}$ |
| $p$ | $\rho_{ref}a^2$ |
| $T$ | $T_{ref}$ |
| $e$ | $a^2$ |
| $k$ | $a^2$ |
| $\varepsilon$ | $a^3/L_{ref}$ |

Table 1. Flow Variable Nondimensionalizing Parameters

Instead of carrying the Reynolds number ($Re$) throughout the computation explicitly, BASS lumps it into the viscosity, $ie$ $\mu_L^* = \mu^*/Re_{ref}$. Doing so makes the NDNSE identical in form to their dimensional counterparts. It must also be kept in mind that the reference $Re$ is based on the speed of sound, not the actual velocity that the computations are run at.

Because the resolution of an acoustic field calls for a detailed simulation of compressible flow (Anderson *et al.* 2005), the equations in (1.4) are spatially Favre-

filtered to obtain the large-eddy simulation equations. In conservation form, the

continuity, momentum, and energy equations are,

$$
\begin{aligned}
&\overline{\rho}_{,t} + \left(\overline{\rho\widetilde{u}_i}\right)_{,i} = 0 \\
&\left(\overline{\rho\widetilde{u}_i}\right)_{,t} + \left(\overline{\rho\widetilde{u}_i\widetilde{u}_j}\right)_{,j} = -\overline{p}_{,i} + \overline{\sigma}_{ij,j} + \tau_{ij,j} \\
&\widetilde{E}_{t,t} = \left[\widetilde{u}_i\left(\widetilde{E}_t + \overline{p}\right)\right]_{,j} - \left(\frac{\mu_L}{(\gamma-1)\mathrm{Pr}_L}\widetilde{T}_{,j} + q_j\right)_{,j} + \left[\widetilde{u}_i\left(\overline{\sigma}_{ij} + \tau_{ij}\right)\right]_{,j}
\end{aligned}
\tag{1.15}
$$

Above, $\overline{\sigma}_{ij}$ and $\tau_{ij}$ are the Favre-filtered viscous stress tensor and subgrid-scale viscous

stress tensor, respectively, and $q_j$ subgrid heat flux. They are defined by the following,

$$
\begin{aligned}
&\overline{\sigma}_{ij} = \mu\left(2\widetilde{S}_{ij} - \frac{2}{3}\widetilde{S}_{mm}\delta_{ij}\right) \\
&\tau_{ij} = \mu_T\left(2\widetilde{S}_{ij} - \frac{2}{3}\widetilde{S}_{mm}\delta_{ij}\right) - \frac{2}{3}\overline{\rho}k\delta_{ij} \\
&q_j = \frac{\mu_T}{\mathrm{Pr}_T}\widetilde{T}_{,j}
\end{aligned}
\tag{1.16}
$$

This system is closed by obtaining $k$ and the eddy viscosity, $\mu_T$, form the two-equation

model as described above and formulating the Favre-filtered strain rate tensors as

$$
\widetilde{S}_{ij} = \frac{1}{2}\left(\widetilde{u}_{i,j} + \widetilde{u}_{j,i}\right).
$$

The governing equations are finally transformed to a general curvilinear

coordinate system by the following:

$$
\begin{aligned}
\xi &= \xi(x,y,z,t) \\
\eta &= \eta(x,y,z,t) \\
\zeta &= \zeta(x,y,z,t) \\
\tau &= \tau(t)
\end{aligned}
\tag{1.17}
$$

In addition, BASS is designed to run on distributed-memory parallel computers with the

use of message passing, greatly reducing user time.

Another fact that reflects the code's robustness is the amount of options the user has to perform the numerical computation. For time-stepping schemes, BASS incorporates Hu *et al.*'s (1996) 5-6 low dispersion and dissipation Runge-Kutta method, several other lower order Runge-Kutta schemes, an implicit scheme, and several Adams-Bashforth schemes. Spatial derivative methods include Tam and Webb's (1993) dispersion-relation preserving (*DRP*) scheme, Hixon's (2000) sixth-order prefactored compact scheme, and sixth- and second-order explicit schemes.

The work done here did not require an incredibly accurate numerical scheme. Going back to the nature of CFD, the mean-flow results being sought would still be of adequate accuracy even if any one of the lower-order schemes are used. Because of this, the second-order explicit scheme in conjunction with a fourth-order Runge-Kutta time stepping was chosen. This then contributes to faster computer time, again, at expense of some numerical accuracy

**Goal of Thesis**

The numerical code used in this work is NASA's BASS code and currently has implemented the high-Reynolds number model described above. Our goal is to modify this model in order to add the capability of handling wall-bounded flows to the code. The specifics of the procedures entail the verification of the code's viscous solving routines as well as the modification of several key modules. Both will be presented in later sections.

# CHAPTER II

## NUMERICAL SIMULATION OF VISCOUS FLOWS

The numerical solution of viscous flows will be discussed in the present chapter. Much, if not all, of the research being done with BASS has concentrated on the use of the Euler equations. As such, the viscous terms incorporated into the code have not been used extensively or been validated. If turbulence is to be analyzed with this platform, the first step in conducting that analysis is verifying that the viscous terms are implemented correctly in the code.

Some simple viscous flow patterns were run. These flows have known analytical solutions which allowed for a direct comparison to be made. The first was a boundary layer solution with zero-pressure gradient. The analytical solution to this pattern was developed long ago by Blasius. The second case was that of fully-developed channel flow. Both will be discussed next.

### Blasius Solution

Boundary layers can vary greatly in size and structure depending on the surface it develops on. The simplest boundary layer flow is encountered in a flow of incompressible, viscous fluid past a long flat plate aligned with the streamlines, Figure 2. In such a situation, the flow in the far-field is essentially inviscid while fluid particles that

enter the boundary layer experience distortions caused by the velocity gradient in the region close to the wall.
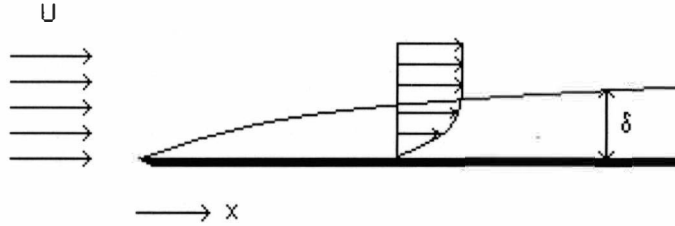


Figure 2. Incompressible, Viscous Flow Past a Long Flat Plate.

The boundary conditions for this flow demand that the velocities at the edge of the boundary layer reach that of the free-stream,

$$u(x \geq 0, y \to \infty) = U_\infty \tag{2.1}$$

where $U_\infty$ is the free-stream velocity. Additionally, the no-slip condition must also be enforced,

$$\begin{aligned} u(x > 0, y = 0) &= 0 \\ v(x > 0, y = 0) &= 0 \end{aligned} \tag{2.2}$$

In actuality, there is no sharp interface between the boundary layer and the free-stream. The velocities shift seamlessly into the free-stream magnitude. Because of this, an exact definition for the boundary layer thickness, $\delta$ in Figure 2, is hard to discern and is typically approximated by,

$$\delta = y \quad \text{where} \quad u = 0.99 U_\infty$$

This magnitude is quite arbitrary. If one compares the boundary layer profile to an inviscid flow over the same plate at the same velocity, one can get a handle on more meaningful thicknesses.

The displacement thickness, $\delta^*$, can be determined by comparing the flow-rate across a particular station on the plate, say b-b in Figure 3. Because of the velocity gradient inside the boundary layer, there will be a velocity deficit, $U - u$. This velocity deficit in turn reduces the flow-rate across the section b-b when compared to the same flow in inviscid conditions, section a-a. If the plate at section a-a is displaced vertically by a certain amount, $\delta^*$, the shaded areas across both stations would be exactly the same. Mathematically, this can be expressed as,

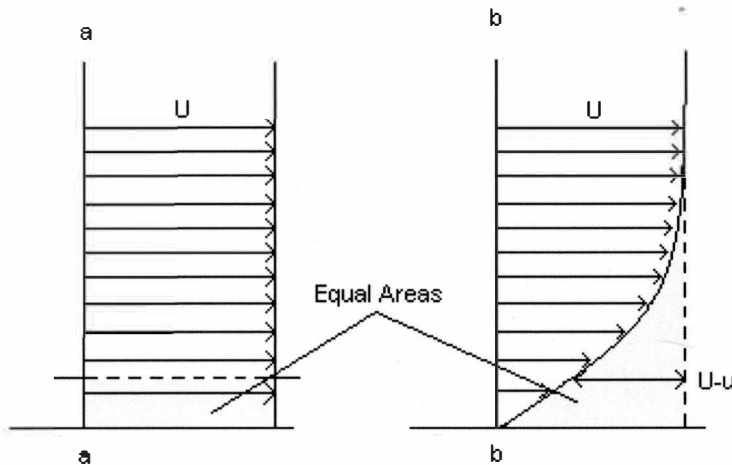$$\delta^* = \int_0^\infty \left(1 - \frac{u}{U_\infty}\right) dy \qquad (2.3)$$



Figure 3. Boundary Layer Displacement Thickness.

What the displacement thickness actually represents is the outward displacement of the streamlines because of the viscous effects from the wall (Munson *et al.* 1998).

Similarly, a thickness based on the momentum flux can also be determined. The momentum thickness, $\Theta$, describes how much vertical displacement a plate in inviscid flow needs go through in order to attain the same momentum flux as in a viscous at the same velocity. Mathematically,

$$\Theta = \int_0^\infty \frac{u}{U_\infty}\left(1 - \frac{u}{U_\infty}\right)dy \tag{2.4}$$

One thing to note about these boundary layer concepts is that they are based on the fact that a boundary layer is thin. This means that anywhere along the plate, $\delta \ll x$, and the same is true for the other thicknesses. These expressions hold as long as the analysis does not get too close to the leading edge of the plate.

The Navier-Stokes can be used to describe the flow past a plate. With the boundary conditions specified in (2.1) and (2.2) and with the assumptions of incompressible flow and that the velocities as well as the rates of change in the wall-normal direction are negligible, the equations reduce to the following,

$$\frac{\partial u}{\partial x} + \frac{\partial v}{\partial y} = 0$$
$$u\frac{\partial u}{\partial x} + v\frac{\partial u}{\partial y} = \nu\frac{\partial^2 u}{\partial y^2} \tag{2.5}$$

These nonlinear partial differential equations were first solved by H. Blasius in 1908. Because of their nonlinear nature, equations (2.5) have no closed-form solution. Instead, Blasius developed a similarity solution. Because neither x nor y have a clear measuring scale inside a boundary layer, many suspect that the solution is strictly

dependent upon a combination of both, *ie* $u(x, y)$ (Panton 1996). Blasius used this fact and the fact that the flow in the y-direction is dominated by a diffusion process to develop his similarity variable,

$$\eta = \frac{y}{\sqrt{\nu L/U\infty}} \qquad (2.6)$$

where L is taken to be the length of the plate.

With this similarity variable, Blasius was able to reduce the problem of a nonlinear partial differential equation into an ordinary differential equation. However, even though the complexity of partial differential equations has been avoided, the ordinary differential equation the results still does not have a closed form solution. Numerical analysis tools were then necessary for the solution of this problem.

Experiments and numerical results confirm that the boundary layer thickness, or the y-coordinate at which the velocity comes within a one percent difference from the free-stream value, occurs at an $\eta \approx 5$. Substituting this into equation (2.6), the boundary layer thickness can be approximated by the following expression,

$$\delta = \frac{5.0x}{\sqrt{Re_x}} \qquad (2.7)$$

with $Re_x = U_\infty x / \nu$, x being longitudinal coordinate, and $\nu$ the kinematic viscosity. The displacement and momentum thicknesses, as well as the coefficient of friction, are then given by,

$$\delta^* = \frac{1.721x}{\sqrt{Re_x}} \qquad \Theta = \frac{0.664x}{\sqrt{Re_x}} \qquad C_f = \frac{0.644}{\sqrt{Re_x}} \qquad (2.8)$$

In its general form, the dimensionless skin friction coefficient is defined as the ratio of wall shear stress to dynamic pressure.

## Numerical Solution

A Blasius solution is steady-state, meaning it does not change with time once the boundary layer develops as long as no external forces act upon it. Unsteady, compressible flow solvers such as BASS are capable of computing steady-state solutions. This is done by simply marching in time while keeping an eye on the evolution of the flow parameters to judge convergence.

To do this, a new module was written and incorporated into the code. First, whereas the code originally overwrote the flow data on subsequent iterations, it was necessary to keep some record of the previous history, mainly the primitive variables at a previous iteration. Having data at two different time levels allowed us to judge how the flow is behaving and whether or not it is reaching steady-state.

A residual was used to judge convergence,

$$R = \frac{1}{N}\sum\left(\frac{\left|\rho_i^{n+1} - \rho_i^n\right|}{\rho_i^n} + \frac{\left|u_i^{n+1} - u_i^n\right|}{u_i^n} + \frac{\left|v_i^{n+1} - v_i^n\right|}{v_i^n} + \frac{\left|w_i^{n+1} - w_i^n\right|}{w_i^n} + \frac{\left|E_{ti}^{n+1} - E_{ti}^n\right|}{E_{ti}^n}\right) \quad (2.9)$$

where, $N$ is the total number of grid points. A convergence criterion needs to be assigned so as to compare it to the residual on each pass. This residual, as well as the evolution of each variable, is output to screen. As an example, Figure 4 shows a plot for the residual versus number of iterations for one of the turbulent runs to be presented later.

As stated earlier, $v$-velocities in boundary layer flow over a flat plate are usually very small. This causes problems in the judging of convergence by the above expression.

If the variations of $v$ are smaller than machine precision, whatever is used in the calculation is completely wrong and hence contributes a lot of error. For example, in the runs completed for the flat plate, the magnitude of these transverse velocities ranged anywhere from $10^{-16}$ to $10^{-30}$; both are well beyond the accuracy of the computer. Because of this, the $v$-velocities added quite a lot of instabilities into the residual computation and were left out of the computation.
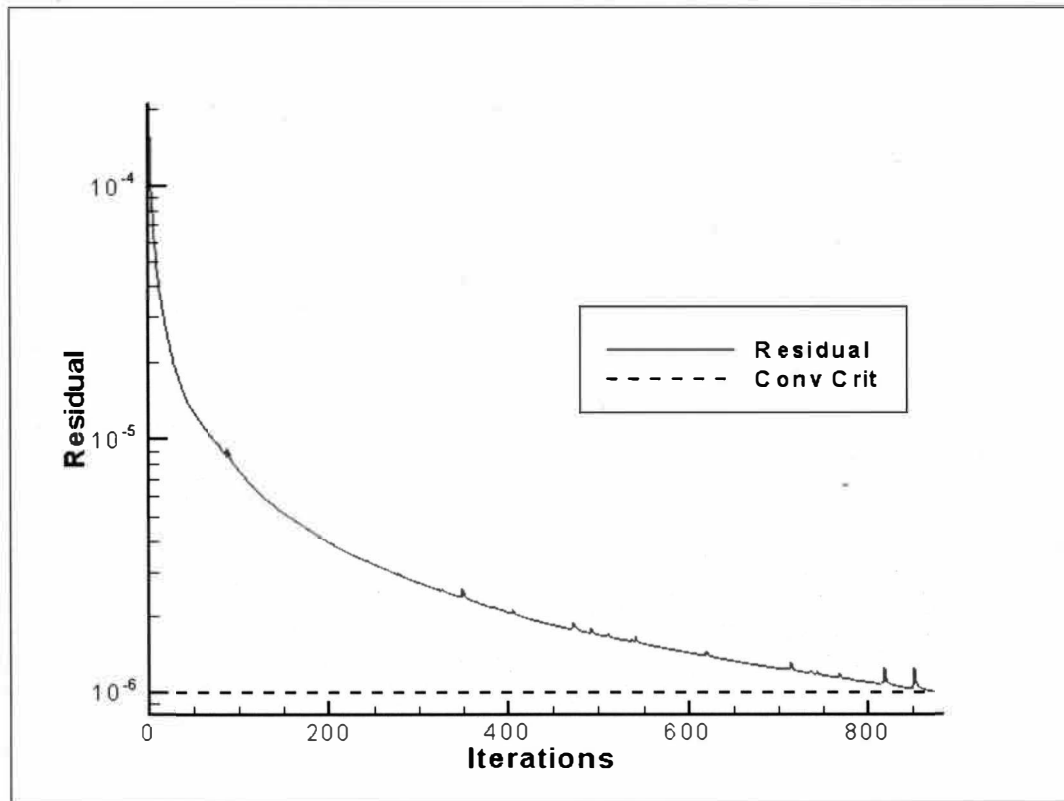


Figure 4. Evolution of the Residual for a Case Run in BASS.

## Grid Development

Now that the code has been set up to handle steady-state, the actual computation of the flow can be started. The first step in any numerical solution is the discretization of

the space of interest by developing an appropriate grid. A simple FORTRAN algorithm was written to develop simple, structured grids. Figure 5 illustrates the different iterations of the grids used throughout the course of this work.

Figure 5a was the initial grid developed and was not without problems. Instead of having a fully-horizontal grid, an attempt was made to slope the y-spacing in the downstream direction. As is evident, there is very little apparent slope in this grid and if one looks more closely into grid, there were problems with spacing (Figure 6a). The sudden jump visible inside the black circle could be cause for computational errors later on because of the difference in subsequent grid metric magnitudes. These two possible sources of error were corrected in the next grid (Figure 5b and Figure 6b).

In Figures 5b and 5d, the actual plate takes up the entire x-domian at $y=0$. This has some disadvantages that will be presented in the results section. The last grid that was used (Figure 5c) placed the plate in the middle of the domain. The advantage of this grid was that it allowed the initialization of the entire domain to a constant flow while producing good results. The disadvantage was that it would be harder to analyze the phenomena of interest since the plate may not be long enough for the development of a Blasius solution. In the end, Figure 5d was chosen and has a grid density of 101-by-101 grid points in a single block.

## Initial and Boundary Conditions

The imposition of a wall boundary condition is paramount in this computation in order to obtain the desired profiles. The wall condition programmed in BASS is that of

Tam and Dong (1994) where the time derivative of the velocity normal to the wall is set to zero,

$$(\rho v)_{,t} = 0 \tag{2.10}$$

This derivative must be expanded in order to accomplish this:

$$(\rho uv)_{,x} + (\rho v^2 + p)_{,y} = v\left[(\rho u)_{,x} + (\rho v)_{,y}\right]$$
$$+ (\rho u)v_{,x} + (\rho v)v_{,y} + p_{,y} = p_{,y} = 0 \tag{2.11}$$
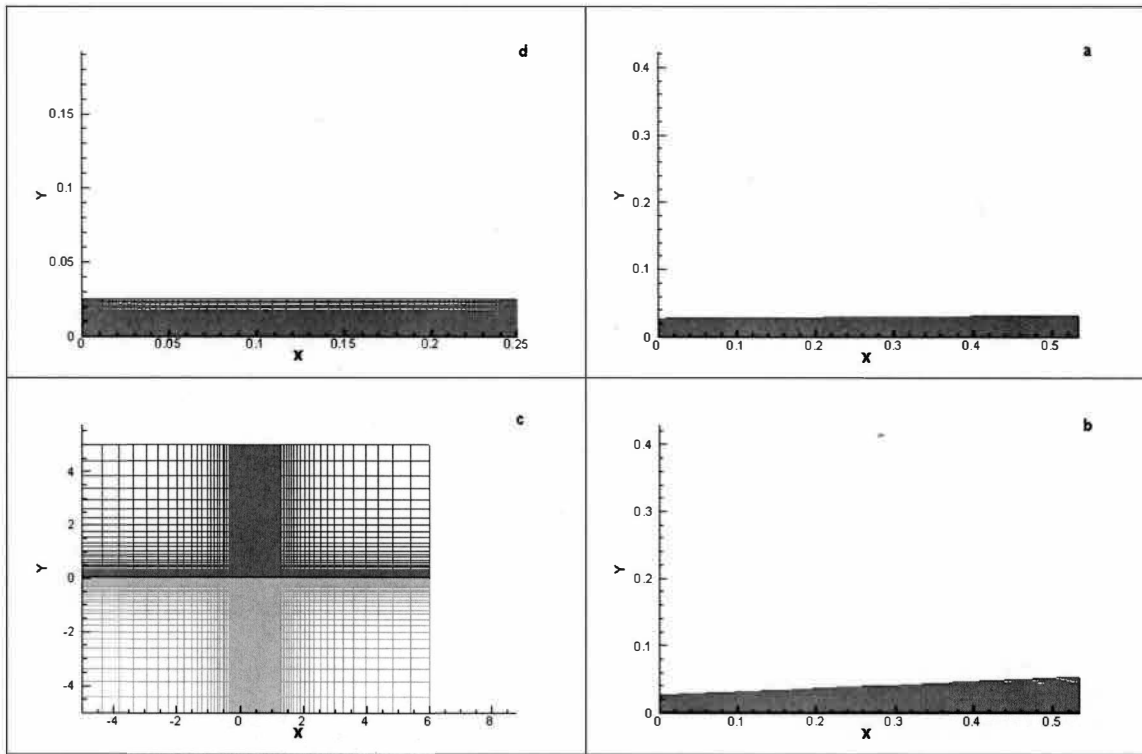


Figure 5. Boundary Layer Grid Iterations.

Finally, the setting of the normal pressure derivative to zero is done by using a ghost point inside the wall.

Thompson boundary conditions (Thompson 1987 and 1990) were used to define the inflow, outflow, and far-field boundaries. In his conditions, Thompson performed one-dimensional characteristic analysis of the Euler equations by considering all transverse terms as being nothing more than constant source terms. Therefore, the conditions are applied only to the derivatives normal to the boundary.
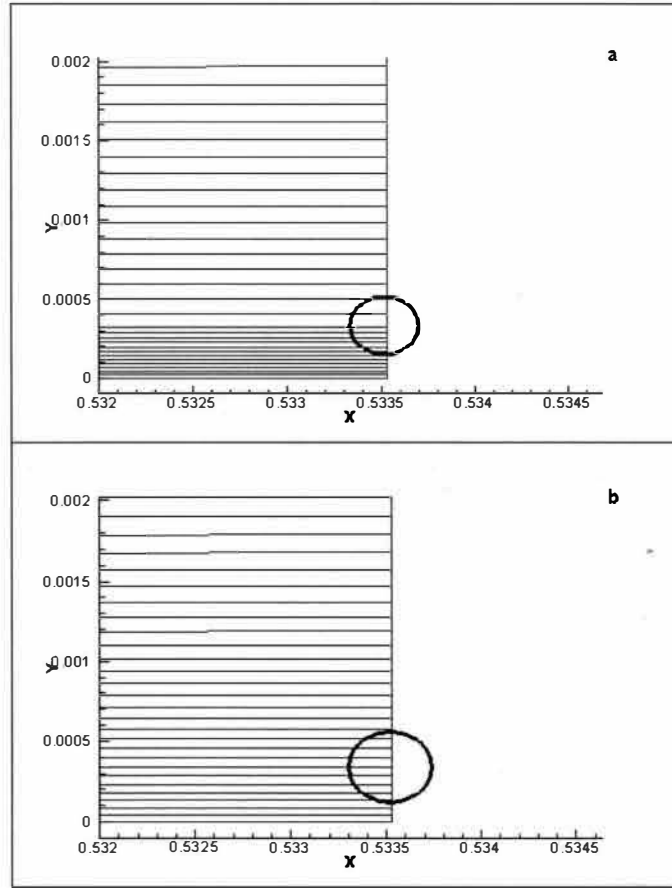


Figure 6. Close-up of Grid Metric Difficulties in Initial Grid.

The one-dimensional characteristics are then determined by linearizing the normal flux derivative term and decomposing it to obtain the characteristic waves:

$$
\begin{aligned}
&(c_1)_t + (\overline{u} - \overline{c})(p_x' - \overline{\rho c}\, u_x') = 0 \qquad (c_3)_t + \overline{u}\, v_x' = 0 \\
&(c_2)_t + \overline{u}(\overline{c}^2 \rho_x' - p_x') = 0 \qquad\qquad (c_4)_t + (\overline{u} + \overline{c})(p_x' + \overline{\rho c}\, u_x') = 0
\end{aligned}
\tag{2.12}
$$

where $c$ denotes the speed of sound and $(\ \bar{}\ )$ represents a mean value. Therefore, at the outflow boundary,

$$\rho' = \rho - \bar{\rho} \qquad v' = v - \bar{v}$$
$$u' = u - \bar{u} \qquad p' = p - \bar{p} \tag{2.13}$$

These characteristics determine the direction in which the flow is traveling. The amplitudes of the characteristics traveling out of the domain are determined by the flow variables; those coming in are specified as boundary conditions and are usually set to zero.

The time derivative of the primitive flow variables can then be calculated after the characteristics are determined,

$$\rho_t = \frac{2(c_2)_t + (c_1)_t + (c_4)_t}{2\bar{c}^2} \qquad v_t = (c_3)_t$$
$$u_t = \frac{(c_4)_t - (c_1)_t}{2\bar{\rho}c} \qquad p_t = \frac{(c_1)_t + (c_4)_t}{2} \tag{2.14}$$

With these variables known, the time derivative of the conserved variables can then be calculated.

As for initial conditions, BASS gives the user two options to specify these. The simplest one is initializing the space to a constant flow, *ie* the user indicates a constant value for the primitive flow variables and the code updates the entire space to these values. The second option calls for the user to input a file containing the values of all the conserved variables, $\rho$, $\rho u$, $\rho v$, $\rho w$, and $E_t$, at each point in the domain. Regarding the Thompson boundary conditions, BASS also requires that the user specify initially the value of the mean primitive variables used for the calculation of the characteristics. As

with the flow initial conditions, these can be specified either as constant or with an input file.

## Results

The first test cases were initialized with a constant flow and constant mean-flow conditions at the inflow and outflow boundaries. This combination proved to be quite troublesome. It has been well documented that inflow Thompson boundary conditions can be unstable and generate random fluctuations that degrades the solution accuracy (Hixon *et al.* 1995). A point in fact is the results of Hixon *et al.* (2000) in which they tested several radiation and outflow boundary conditions in a cascade problem. It was concluded that the reflections from Thompson's inflow conditions interacted with the cascade and created a feedback loop which in turn caused an unrealistic rapid build up of pressure.

This same problem is evident in our computation with the constant initial flow. Figure 7 depicts the corner of the domain where the inflow and wall conditions interact. After 4000 iterations, the pressure had increased by 14 percent and was still increasing. At the outflow, the complete opposite occurs. Here, instead of a steady increase, the Thompson-wall interaction acts like a sink, reducing the pressure and further distorting the flow pattern.

To overcome this problem, an initial flow file was developed in order to give BASS a better starting point for its computation. A Reynolds number based on momentum thickness ($Re_\Theta$) greater than zero was chosen so as to get away from the numerical singularity caused by the edge of the plate. With this Reynolds number, an

approximation to the Blasius solution was developed and used as the initial condition.

Files for the mean-flow variables at the radiation boundary conditions were also
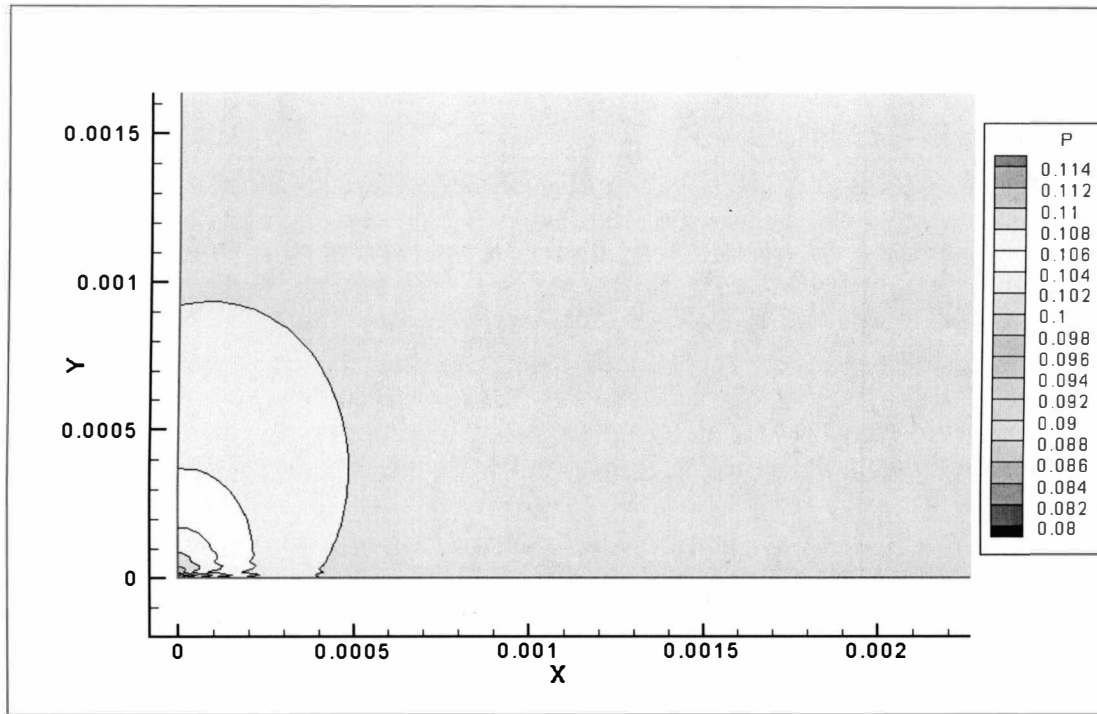


Figure 7. Pressure Buildup with Thompson Inflow and Wall Boundary Conditions.

developed in the same way. These approximations greatly enhanced the computation and

it converged within several iterations.

Figures 8 through 11 show the comparison between the numerical and Blasius

solutions for the boundary layer thicknesses and the skin friction coefficient. There was

decent agreement for all of the parameters but they seem to be somewhat slower than the

Blasius solution. Still, the deviations are less than around 2 percent. The half-meter-long

plate used in the computations allowed for a rather good similarity solution, as can be

seen in Figure 12 (Schlichting, 1979), and offered a wide range of Reynolds numbers

$(Re_x)$.
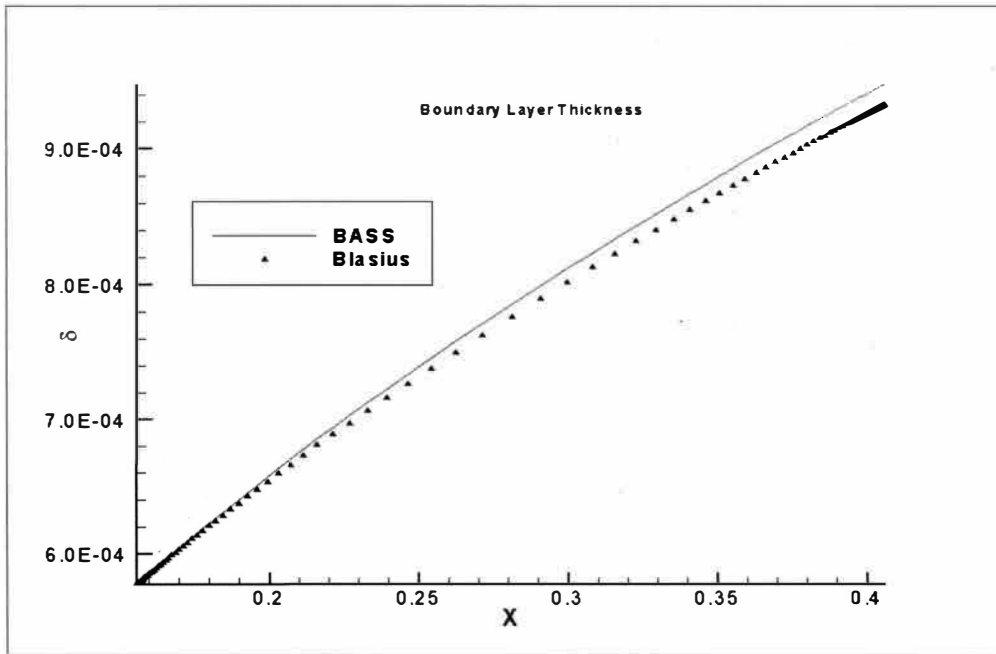
Figure 8. Comparison of Boundary Layer Thicknesses ($\delta$).
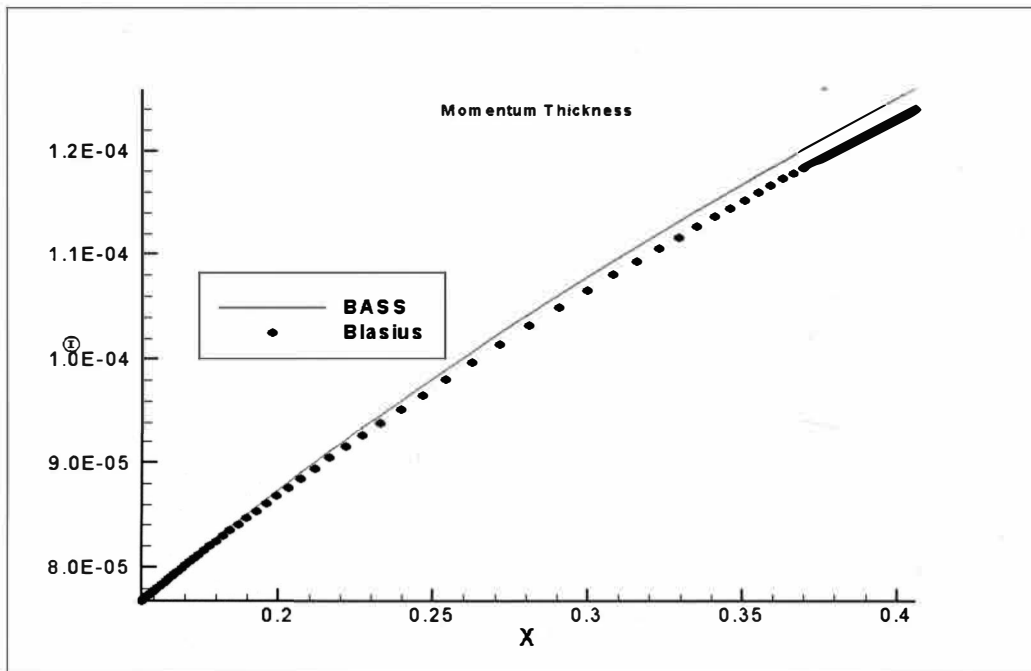


Figure 9. Comparison of Momentum Thicknesses ($\Theta$).
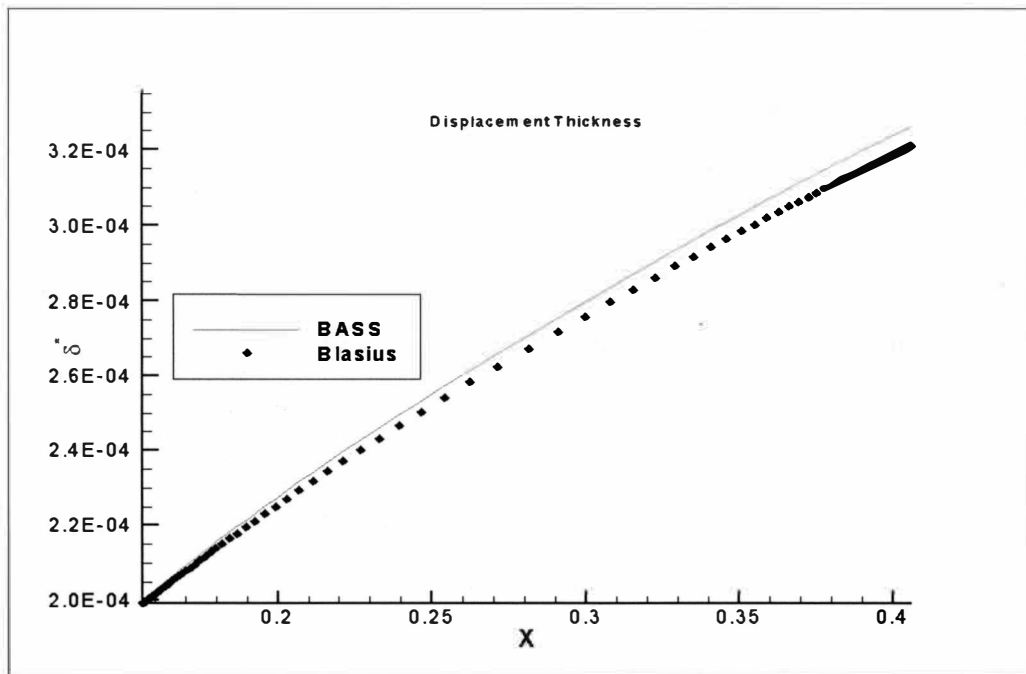
Figure 10. Displacement Thickness ($\delta^*$) Comparisons.

Any initialization that varied substantially from a Blasius solution ran into problems, making the code extremely sensitive to initial conditions. Thanks to the initializations used, however, the pressure disturbances associated with the boundary conditions were never given enough time to develop and degrade the solution. This procedure may not always be the best approach or be feasible. Since the code was developed to solve flows in complex geometries, it is likely that an initialization for a simulation in such conditions will not be known *a priori*, so using an initial constant flow would be the only option for the experimenter. Because of this, the development of accurate boundary conditions near walls is still a topic of much debate and research.
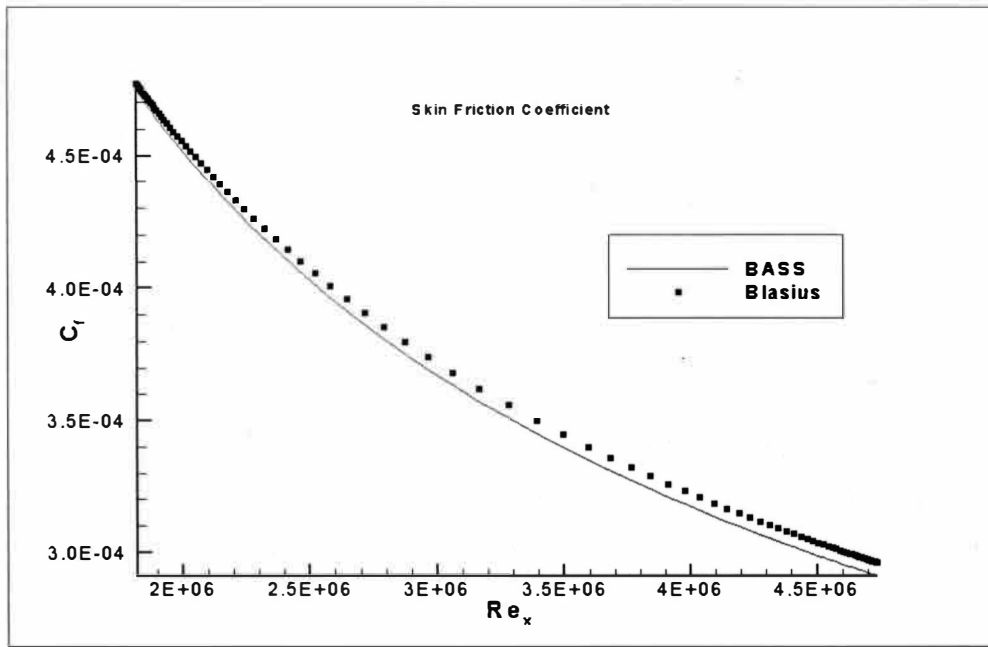
Figure 11. Comparison of Skin Friction Coefficients ($C_f$).
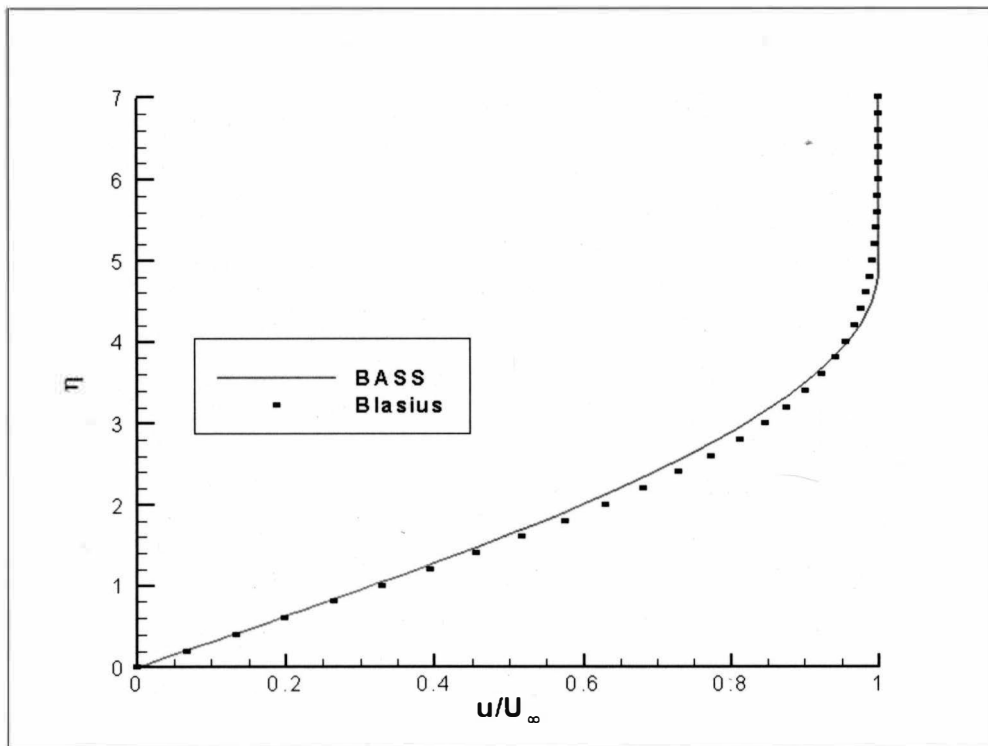


Figure 12. Nondimensional Boundary Layer Velocity Profiles.

31

# Laminar Channel Flow

Viscous flow between two horizontal, infinite plates will be looked at next (Figure 13). As with laminar boundary layers, the flow is assumed incompressible. In this regime, the flow is driven by a pressure gradient in the longitudinal direction and it
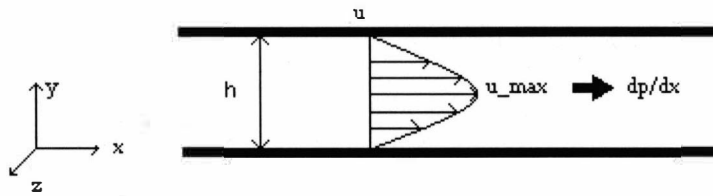


Figure 13. Pressure-Driven Flow between Parallel Plates.

is known that there is no velocity in the y- or z-direction. From the continuity equation, Equation (1.1), it follows that $\partial u / \partial x = 0$. Substituting these into the Navier-Stokes equations and considering the channel height, $h$, the governing equations reduce to the following,

$$0 = -\frac{\partial p}{\partial x} + \mu \left( \frac{\partial^2 u}{\partial y^2} \right)$$

$$0 = -\frac{\partial p}{\partial y} - \rho g \qquad\qquad (2.15)$$

$$0 = -\frac{\partial p}{\partial z}$$

For this equations, steady state was assumed, *ie* $\partial u / \partial t = 0$, and $g$ is the gravitational force.

Integrating the above equations yields,

$$p = -\rho g y + f_1(x)$$

$$u = \frac{1}{2\mu}\left(\frac{\partial p}{\partial x}\right)y^2 + c_1 y + c_2 \tag{2.16}$$

where the pressure is shown to vary hydrostatically in the y-direction, $c_1$ and $c_2$ are

integration constants, and $f_1$ is a function to be determined. The dependency of pressure

in the y-coordinate was eliminated by assuming the height of the channel was negligible

when compared to the length.

No-slip boundary conditions were used at both walls to close the above equations,

$$u(x, y = 0) = 0$$

$$u(x, y = h) = 0 \tag{2.17}$$

To satisfy these conditions $c_2 = 0$ and $c_1 = -\frac{1}{2\mu}\frac{dp}{dx}h$. With the value of the constants

known, the governing equations for laminar channel flow are,

$$u(y) = \frac{1}{2\mu}\frac{dp}{dx}\left[y(y-h)\right]$$

$$p = \left(\frac{dp}{dx}\right)x + p_o \tag{2.18}$$

where $p_o$ is the reference pressure at $x = y = 0$. Notice that since $p$ is a function of $x$ only,

the partial differentiation reduced to an ordinary one.

## Results

For the numerical computation, a grid for a channel just over 2.0 meters in length

and approximately 0.04 meters in height was developed. Figure 14, below, illustrates the

grid, which has a density of 201-by-101 points. This numerical solution is more

forgiving than the plate since it does not have to worry about the interactions of a

developing boundary layer or the effects of the far-field. The presence of the two walls

makes for an easier solution. However, the same problems with regards to the boundaries are present.

As with the boundary layer flow, the approach taken was to develop initial flow files based on approximations to the analytical solution. Results are in excellent agreement as can be seen in Figure 15. Again, the flow converged rather quickly and did not allow the pressure to build up. This build-up could have potentially been more severe here than in the boundary layer because of the fact that there are two walls present, creating twice as many pressure sources that can alter the streamlines.
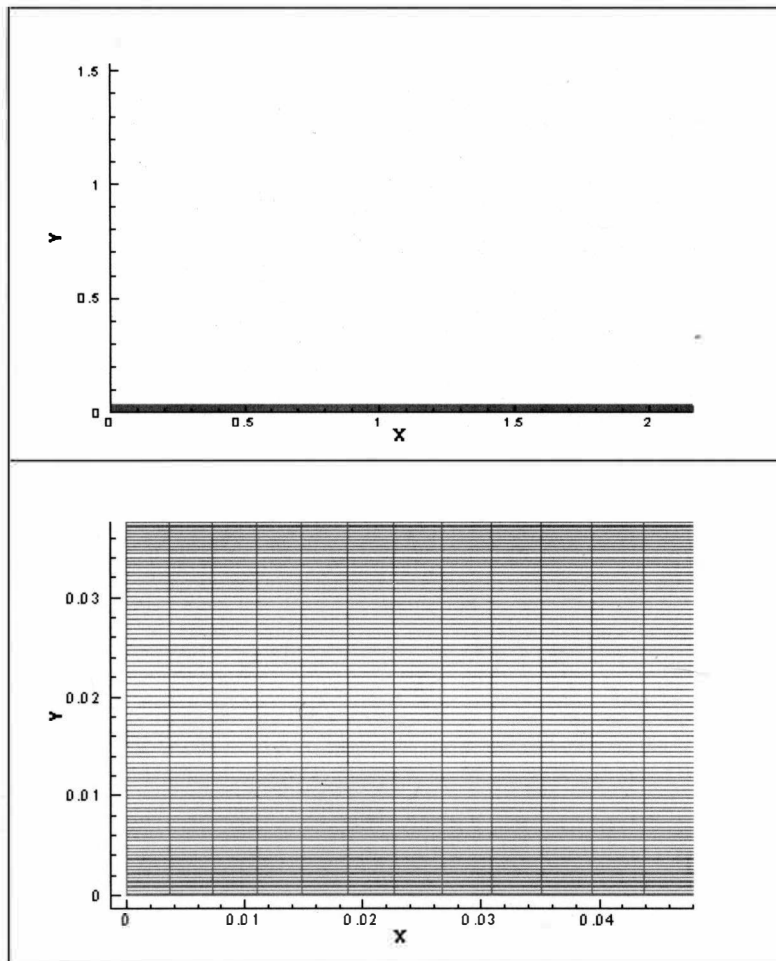


Figure 14. Laminar Channel Flow Grid.

The black curve in the Figure 15 represents the analytical parabolic profile expected. It is evident that the solutions at the various speeds run agree well with the profile. The Reynolds numbers indicated are based on the channel height, $h$.
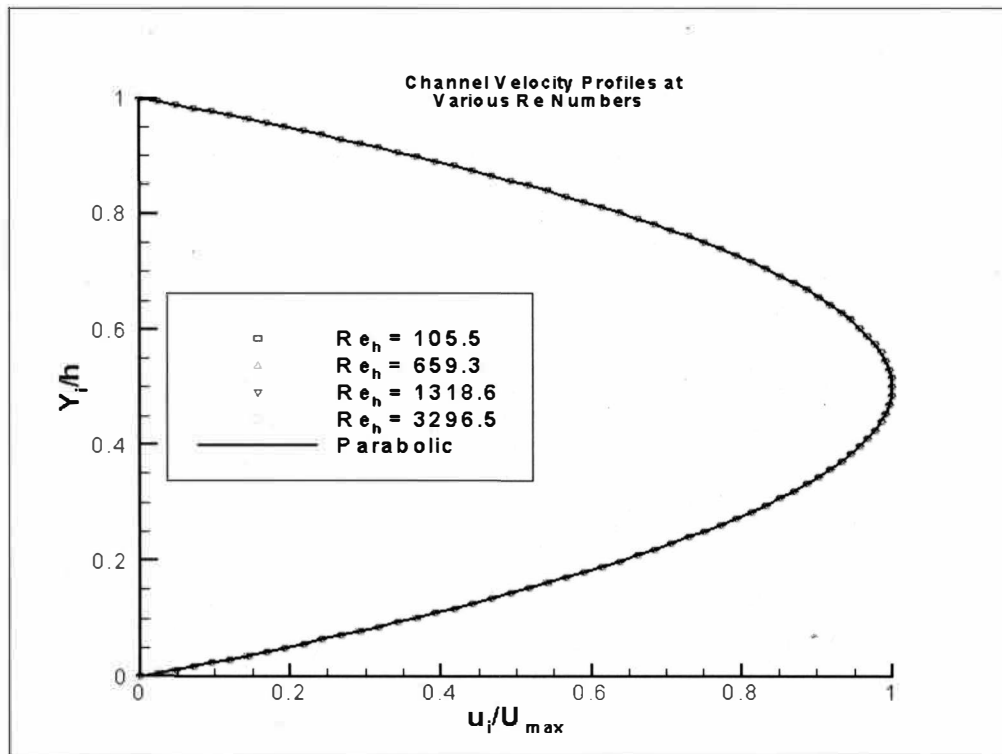


Figure 15. Velocity Profiles for Channel Flow at Various Reynolds Numbers.

## Summary

BASS has been shown to produce usable results for analyzing viscous flows once it has been modified to acquire steady-state solutions by the method discussed in Chapter I. With the exception of its difficulties in the initialization phase with a constant flow, the code performed extremely well. It was just a matter of identifying how sensitive it was to initial conditions and giving it workable profiles for it to work from. The maximum error

was seen to occur in the calculation of the displacement thickness in the boundary layer but was never greater than 5 percent.

# CHAPTER III

## LOW-REYNOLDS NUMBER TURBULENCE

Turbulent flows can be very different from one another. In Chapter I, several characteristics shared by all turbulent flows were highlighted, chief among these being the associated randomness and high Reynolds numbers. These flows can be classified into three different groups: grid-like flows, free-shear flows, and wall layers. The first two share certain qualities that greatly simplify their analysis. Wall layers, on the other hand, present challenging complications that render most of the analysis developed for free-shear flows and grid-like turbulence invalid. In this chapter, the procedure used to modify BASS to handle wall-bounded flows and its associated phenomena is highlighted as well as a brief overview on the specifics of the complications presented by a wall.

### Wall-Bounded Flows

Everyone is familiar with the plume of smoke coming from any chimney. Like cigarette smoke, it starts out as laminar flow and instabilities quickly get magnified and cause the flow to become turbulent. In these examples, the flows can be classified as free-shears since there are no physical constraints hindering the development of the flow. As in most turbulent flows, high Reynolds numbers are associated with free-turbulence and the flow then carries with it a great range in eddy size. Additionally, in these high

Reynolds numbers, viscous effects on the development and behavior of the overall flow can be neglected (Hinze, 1975).

It is known that the small-scales in turbulence continuously extract energy from the mean flow. These small scales are close to being *isotropic*, or rather; the flow at these scales has mean properties that are independent of the direction of the axes of reference. This, in turn, allows us to make significant simplifications to the governing equations.

In wall layers, however, the assumptions of isotropic turbulence and homogeneity, or that the turbulence mean properties are independent of position, are questionable. Since many turbulence models use these two assumptions as a cornerstone in their development, many need to be modified substantially in order to accurately model wall-bounded flows. To look at the effects of walls, the simplest wall-bounded flow, that of incompressible turbulent flow in a channel, will be discussed briefly.

Before going into this discussion on the flow dynamics, it is prudent to point out that most of the analyses done on wall flows have used the incompressible Reynolds-Averaged Navier-Stokes (*RANS*) equations as the governing equations. Therefore, for the sake of completeness, the *RANS* equations are presented here. In these equations, the flow variables are decomposed into a mean and a fluctuating part, *ie* $\phi = \Phi + \phi'$, where $\Phi$ is the mean value, $\phi'$ the fluctuating part, and $\phi$ the total value. Inserting this decomposition into Equations (1.1-1.3) and accounting for incompressibility yields:

Continuity:

$$\frac{\partial U_i}{\partial x_i} = 0 \qquad\qquad (3.1)$$

Momentum:

$$\rho \frac{DU_i}{Dt} = \rho G_i - \frac{\partial P}{\partial x_i} + \frac{\partial \tau_{ij}}{\partial x_j} + \frac{\partial \tau'_{ij}}{\partial x_j} \qquad (3.2)$$

Energy:

$$\rho C_p \frac{DT}{Dt} = \tau_{ij} \frac{\partial U_i}{\partial x_j} - \frac{\partial q_i}{\partial x_i} + \frac{\partial q'_i}{\partial x_i} + \Phi' \qquad (3.3)$$

Here, $\tau_{ij}$, $q_i$, $\tau'_{ij}$, and $q'_{ij}$ are the mean and turbulent shear stress and heat flux terms.

These, along with $\Phi^r$ are:

$$\tau_{ij} = \mu \left( \frac{\partial U_i}{\partial x_j} + \frac{\partial U_j}{\partial x_i} \right) \qquad q_i = -k \frac{\partial T}{\partial x_i}$$

$$\tau'_{ij} = -\rho \overline{u_i u_j} \qquad q'_i = -C_p \rho \overline{u_i \theta} \qquad (3.4)$$

$$\Phi' = \overline{\tau'_{ij} \frac{\partial u_i}{\partial x_j}} \qquad \tau'_{ij} = \mu \left( \frac{\partial u_i}{\partial x_j} + \frac{\partial u_j}{\partial x_i} \right)$$

As can be seen, and as is expected, the averaging procedure adds additional terms that account for the effects of the flow parameter fluctuations on the mean flow.

## Channel Turbulence

Perhaps the most important aspect of wall flows is the fact that the no-slip condition must be enforced on both the mean flow and the velocity fluctuations. Because of this, both tangential and wall-normal velocities must be zero at the wall. This creates a very steep velocity gradient near the wall. In addition, all turbulent fluctuations must also go down to zero, which is effectively a hampering of the turbulence processes and can be thought of as a large "sink" for momentum due to the large dissipation inherent in the region (Tennekes and Lumley, 1972).

These considerations give rise to three distinct layers in the region near the wall. Figure 16 shows what a mean velocity profile for flow through a channel typically looks like. The different layers are identified, but note that the figure is *not* to scale. For example, in a flow with a Reynolds number of around $10^5$, the thin viscous layer next to the wall is contained within a height of $y/R \approx 0.001$. In the figure, *VSL*, *BFL*, and *FTL* correspond to the viscous sublayer, buffer layer, and fully-turbulent layer, respectively.
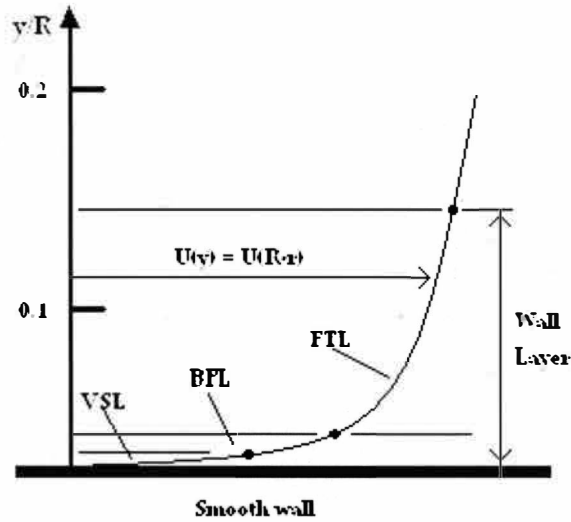


Figure 16. Three-Layer Structure of Mean-Velocity Profiles near Smooth Wall.

As the name implies, the dynamics inside the *viscous* sublayer (*VSL* in Figure 16) are dominated by viscous effects, hence the turbulent stresses, $\tau'_{ij} = -\overline{\rho u_i u_j}$, are negligible because of the velocity fluctuations vanishing at the wall and the region being so thin. Mean velocity variations, therefore, are solely due to the effects from molecular viscosity and, like laminar flows, have a tendency to be linear in this layer. This dominance results in the turbulent Reynolds number, $\mathrm{Re}_T = \rho k^2 / \varepsilon \mu$, dropping significantly, indicating a

strong influence of molecular viscosity on the development of turbulence processes, *ie* production, diffusion, and dissipation (Jones and Launder, 1973).

A characteristic length on the order of $\nu/w$, where $\nu$ is the kinematic viscosity and $w$ a measure of the turbulent velocity fluctuations, is present here. It turns out that this length is much smaller than the length scale associated with the large scale flow which, in the case of channel flow, is the channel half-height, $h$. This is another major complication in wall layers, at least two length scales need to be resolved simultaneously.

Adjacent to the viscous sublayer is the so-called *buffer* layer (*BFL*). In this layer, both the viscous and turbulent stresses are of comparable magnitude. It can be thought of as a transitional phase to the inviscid, turbulent outer flow, *ie* the flow away from the wall.

From Figure 16, it can be seen that the fully-turbulent layer (*FTL*) is still relatively close to the wall. As a matter of fact, the *FTL* is still dominated by wall effects. The only difference from the *BFL* and *VSL* is that here, turbulence has developed to the point of rendering viscous effects ineffective in altering the mean flow (Reynolds, 1974). Here, the large eddies are responsible for friction and turbulence production while in the viscous layer, the small scales dominated these processes as well as the dissipation of energy, which is a continuous process.

In order to obtain some type of approximation to the velocity profiles in these layers, the viscous sublayer and the fully-turbulent regions are typically analyzed separately. This is done because each one has a different asymptotic behavior (Tennekes and Lumley, 1972). In the end, the two descriptions are matched.

41

In the whole of the wall-region, the major parameters that control the development of the flow are the wall stress, $\tau_w$, the viscosity $\mu$, and the fluid density, $\rho$. Therefore, by performing dimensional analysis on the incompressible Navier-Stokes, Equations (3.1-3.4), it can be deduced that the velocity profiles scale with the wall-stress-to-fluid-density ratio, $\tau_w/\rho$. In fact, this ratio has units of velocity-squared and is the basis for the characteristic velocity, $w$, in the definition of the length scale in the viscous region (Hinze, 1975). This velocity scale is termed the *friction velocity* and is defined by:

$$u_\tau = \sqrt{\tau_w/\rho} \qquad (3.5)$$

Again, since the kinematic viscosity is the parameter of most importance, the mean velocity in the x-direction, $U$, must be a function of $u_\tau$, $v$, and $y$:

$$\frac{U}{u_\tau} = f\left(\frac{u_\tau y}{v}\right) \qquad (3.6)$$

Following the necessary boundary conditions, $U$ must be zero at the wall and a linear relationship for its gradient is obtained as y tends to zero ($y \to \infty$). It is further assumed that, in the near-wall region, the size of the eddies is proportional to the distance from the wall (Hinze, 1975). This turns out to be a valid assumption because it is known that in short distances such as those encompassed in these layers, the eddy viscosity will vary linearly with distance so that diffusion of fluid particles is limited to short distances. Mathematically, this translates to:

$$\mu_t = \kappa u_\tau y \qquad (3.7)$$

The equation for the velocity profiles then becomes:

$$\kappa u_\tau y \frac{\partial U}{\partial y} = \frac{\tau_w}{\rho} = u_\tau^2 \tag{3.8}$$

The following nondimensional variables are then introduced into Equation (3.8):

$$U^+ = \frac{U}{u_\tau} \qquad y^+ = \frac{u_\tau y}{\nu} \tag{3.9}$$

resulting in the well-known *Law of the Wall* after integration:

$$U^+ = \frac{1}{\kappa} \ln y^+ + C \tag{3.10}$$

where $\kappa$ and $C$ are constants that depend on the flow situation. Typically, $\kappa$, the von Karman constant, is assigned a value between 0.4 and 0.42, and $C$ is found to be close to 5.0. These two constants were determined by experimental results. Because the mean velocity in the viscous region is known to vary linearly, when the nondimensionalizations in (3.8) are introduced it is found that the velocity profiles closest to the wall vary as:

$$U^+ = y^+ \tag{3.11}$$

The buffer layer proves to be more difficult to model. Because of that, many engineering applications simply assume the profile of (3.11) directly up to point where the curve intersects (3.10), the logarithmic layer equation. Others, like von Karman, have attempted to develop actual expressions for the complex processes involved in the buffer layer. In all, the velocity profile in Figure 16 looks like that in Figure 17 after the nondimensionalization by (3.8).

Even though this discussion has been based on turbulent flow in a channel, the velocity profiles in a turbulent boundary layer with zero-pressure gradient are quite similar to those in a channel flow. Actually, Schlichting (1979) and Prandtl developed their analysis of turbulent boundary layers by assuming that the velocity distribution in

43

boundary layers is identical to those in the channel. This actually proves to be an extremely reasonable assumption that has been verified experimentally up to Reynolds numbers of around one million. What needs to be noted about boundary layers is that they are a combination of both a wall-layer and an outer turbulence developing an
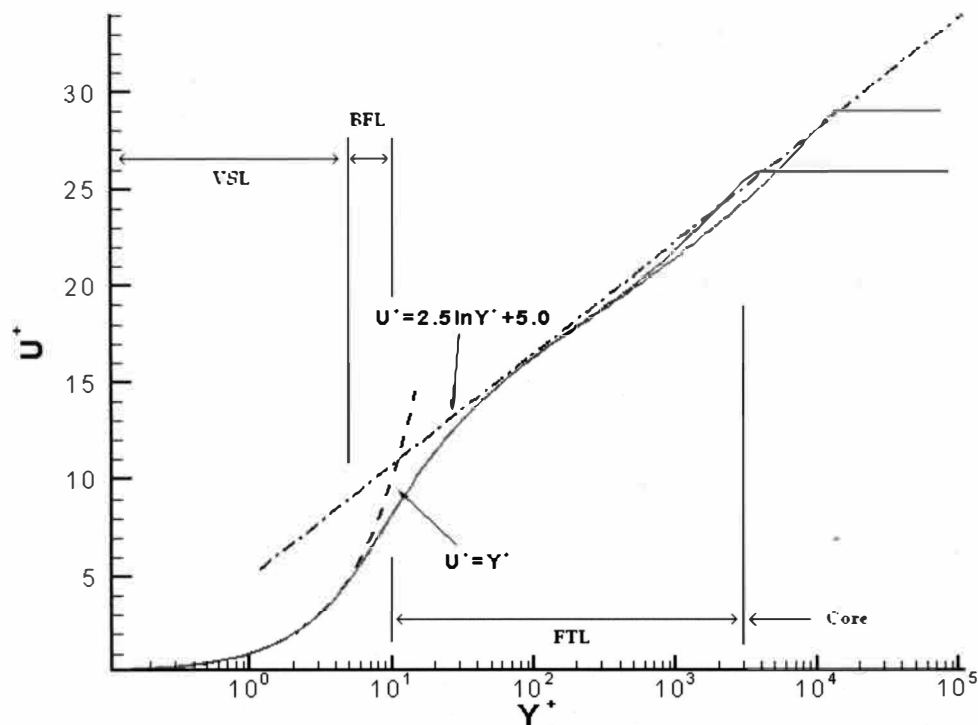


Figure 17. Logarithmic Mean-Velocity Profile.

advancing interface, *ie* the boundary layer thickness increases downstream, and, like in channels and pipes, most of the velocity variation takes place inside the wall-layer (Reynolds, 1974).

44

## Modeling of Wall-Bounded Flows

Having a notion of the phenomena that will have to be resolved in near-wall flows is paramount to the development of adequate turbulence models. Launder and Spaulding (1972) point out several attributes which engineers and model developers strive for. A good turbulence model should:

- be applicable in a wide range of flow conditions;

- be accurate;

- make efficient use of computer memory; and

- be as simple as possible to implement.

The $k$-$\varepsilon$ model that is the focus of this work has become one of the more reliable and widely used turbulence models in engineering applications. It satisfies most of the conditions specified above. However, as pointed out in Chapter I, the standard model does have its downfalls.

Close to walls, the standard $k$-$\varepsilon$ model runs into problems. The reason for this lays in the way the model's dissipation equation was developed. The model was designed for high-Reynolds number flows where the assumption of isotropic turbulence in the small scales is valid. With this assumption, the time scale of turbulence, $T_t = k/\varepsilon$, remains finite. Since the boundary conditions in near-wall flows dictate that both $k$ and $\varepsilon$ must go down to zero at the wall, a singularity is obtained and $k/\varepsilon$ cannot represent the time scale of turbulence anymore (Yang $et$ $al$, 1993).

There have been several procedures developed in order to correct this problem. The first procedure developed was to use empirical equations that describe the variation

of the flow parameters in the region between the wall and the fully-turbulent region

(Chen, 1998).  As a matter of fact, expressions of this sort have already been given in

Equations (3.10 and 3.11).  Figure 18 shows how wall functions can be used to bridge the

gap between the wall and the fully turbulent region in order to allow for the use of the

standard $k-\varepsilon$ model without any other major modifications.  This can be thought of as

specifying the velocity distribution inside the wall layer as Dirichlet boundary conditions

(Henkes, 1998).  This effectively allows the engineer to bypass any uncertainty he may

have on whether or not the turbulence model being used is accurate in the wall region.
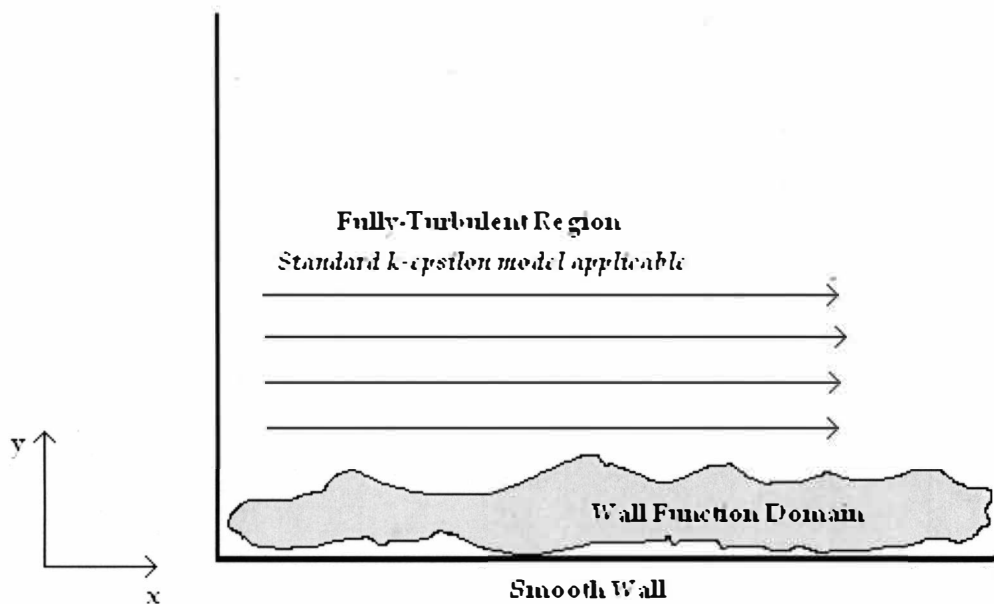


Figure 18.  Wall Function Domain Used in Conjunction with a High-Reynolds Number
       Model.

Still, others may find that resolving the dynamics near the wall are of particular

use to them.  For example, in the design of heat transfer equipment, the engineer would

have to deem it necessary to know as much about near wall turbulence in his design in order to optimize say, a heat exchanger. In this case, integration of the model equations all the way down to the wall is the best approach.

## Two-Equation Near-Wall Modeling

The problem with using wall functions or simple algebraic models for prescription of the length scale is that the variation of this scale is not very accurately resolved. As mentioned in Chapter I, a two-equation turbulence model solves a transport differential equation for a parameter directly related to the length scale and another for the velocity scale, eliminating most of the uncertainty in the validity of the length scale being used. Typically, variables of the form $k^a l^b$, where $a$ and $b$ are constants, are chosen to develop these equations. In this case, the variable $\varepsilon$ is proportional to $\dfrac{k^{3/2}}{l}$.

The transport equations in the standard $k$-$\varepsilon$ model are:

Turbulent Kinetic Energy:

$$
\begin{aligned}
\left(\overline{\rho}\widetilde{k}\right)_{,t} + \left(\overline{\rho}\widetilde{u}_j\widetilde{k}\right)_{,j} &= \left[\left(\mu_T\big/\mathrm{Pr}_k\right)\widetilde{k}_{,k}\right]_{,j} \\
&+ \left[2\mu_T\left(S_{ij} - \frac{1}{3}\delta_{ij}\widetilde{u}_{k,k}\right) - \frac{2}{3}\overline{\rho}\widetilde{k}\,\delta_{ij}\right]\widetilde{u}_{i,j} - \overline{\rho}\widetilde{\varepsilon}
\end{aligned}
\tag{3.12}
$$

Dissipation of Turbulent Kinetic Energy:

$$
\begin{aligned}
\left(\overline{\rho}\widetilde{\varepsilon}\right)_{,t} + \left(\overline{\rho}\widetilde{u}_j\widetilde{\varepsilon}\right)_{,j} &= \left[\left(\mu_T\big/\mathrm{Pr}_\varepsilon\right)\widetilde{\varepsilon}_{,j}\right] \\
&+ C_{\varepsilon 1}\frac{\widetilde{\varepsilon}}{\widetilde{k}}\left[2\mu_T\left(S_{ij} - \frac{1}{3}\delta_{ij}\widetilde{u}_{k,k}\right) - \frac{2}{3}\overline{\rho}\widetilde{k}\,\delta_{ij}\right]\widetilde{u}_{i,j} - C_{\varepsilon 2}\overline{\rho}\frac{\widetilde{\varepsilon}^{\,2}}{\widetilde{k}}
\end{aligned}
\tag{3.13}
$$

The equations are in their compressible-flow form and model the turbulent stresses according to Shih $et\ al$ (1994a), $ie - \overline{\rho u_i u_j} = \mu_t \left( \widetilde{u}_{i,j} + \widetilde{u}_{j,i} \right) - \frac{2}{3} \widetilde{k} \delta_{ij}$.

Jones and Launder (1972) were the first to extend this model's capabilities of computing low-Reynolds number flows. To do this, the model had to be modified in the flowing ways to resolve the appropriate phenomena:

- Viscous diffusion of both $k$ and $\varepsilon$ had to be accounted for in the near-wall region;

- Terms carrying additional constants, $ie\ C_{\varepsilon1}$ and $C_{\varepsilon2}$, must become dependent on turbulent Reynolds number, $\mathrm{Re}_T = \dfrac{\overline{\rho} \widetilde{k}^2}{\widetilde{\varepsilon} \mu}$; and

- Because dissipation will no longer be isotropic, the dissipation equation had to be modified to take this into account.

The model constants also vary between the standard and Jones and Launder's formulations. However, in either case, the first dissipation coefficient, $C_{\varepsilon1}$, is chosen so that the von Karman constant, $\kappa$, attains a value of 0.42 while the second dissipation coefficient, $C_{\varepsilon2}$, is determined from decaying grid turbulence (Jones and Launder, 1973).

Chien's (1982) $k$-$\varepsilon$ model is very similar in structure to that of Jones and Launder's; however, the big difference between the two is that Chien used Taylor series expansions to study the behavior of turbulent fluctuations near the wall. As a result, he arrived at a slightly formulation. His transport equations for the turbulent energy and its dissipation are:

Turbulent Kinetic Energy:

$$\left(\overline{\rho}\widetilde{k}\right)_{,t} + \left(\overline{\rho}\widetilde{u}_j\widetilde{k}\right)_{,j} = \left[\left(\mu + {\mu_T}\big/{\mathrm{Pr}_k}\right)\widetilde{k}_{,k}\right]_{,j}$$
$$+ \left[2\mu_T\left(S_{ij} - \frac{1}{3}\delta_{ij}\widetilde{u}_{k,k}\right) - \frac{2}{3}\overline{\rho}\widetilde{k}\,\delta_{ij}\right]\widetilde{u}_{i,j} - \overline{\rho}\widetilde{\varepsilon} - 2\mu\frac{\widetilde{k}^2}{y^2} \qquad (3.14)$$

Dissipation of Energy:

$$\left(\overline{\rho}\widetilde{\varepsilon}\right)_{,t} + \left(\overline{\rho}\widetilde{u}_j\widetilde{\varepsilon}\right)_{,j} = \left[\left(\mu + {\mu_T}\big/{\mathrm{Pr}_\varepsilon}\right)\widetilde{\varepsilon}_{,j}\right]$$
$$+ C_{\varepsilon 1}\frac{\widetilde{\varepsilon}}{\widetilde{k}}\left[2\mu_T\left(S_{ij} - \frac{1}{3}\delta_{ij}\widetilde{u}_{k,k}\right) - \frac{2}{3}\overline{\rho}\widetilde{k}\,\delta_{ij}\right]\widetilde{u}_{i,j} \qquad (3.15)$$
$$- C_{\varepsilon 2}\overline{\rho}\frac{\widetilde{\varepsilon}^2}{\widetilde{k}} - f_2$$

where the turbulent viscosity is defined as $\mu_T = C_\mu f_\mu \overline{\rho}\,{\widetilde{k}^2}\big/{\widetilde{\varepsilon}}$ .

In this and other similar models, the functions $f$ are wall damping functions used to account for the low-Reynolds number effects. The functions used in the above model are:

$$f_\mu = 1.0 - e^{-0.115 y^+}$$
$$f_1 = 1.0 - 0.22 e^{-(\mathrm{Re}_T/6)^2} \qquad (3.16)$$
$$f_2 = -2\mu\frac{\widetilde{\varepsilon}}{y^2}e^{-y^+/2}$$

Equations (3.14 – 3.16) along with the constants in Table 2 comprise the model chosen to be the platform for low-Reynolds number turbulence modeling in BASS.

| $C_\mu$ | $C_{\varepsilon 1}$ | $C_{\varepsilon 2}$ | $Pr_k$ | $Pr_\varepsilon$ |
|---------|---------------------|---------------------|--------|------------------|
| 0.09 | 1.35 | 1.8 | 1.0 | 1.3 |

Table 2. Model Constants for Chien's $k$-$\varepsilon$ Model.

These constants are different than those of Jones and Launder or even the standard model. Chien, however, argues that since turbulent production and dissipation rates are nearly in balance in wall-bounded flows, the difference between $C_{\varepsilon 1}$ and $C_{\varepsilon 2}$ is the important point and because of this, the difference is kept constant. The corresponding boundary conditions for these equations are:

$$
\begin{aligned}
k(x, y = 0) &= \varepsilon(x, y = 0) = 0 \\
\frac{\partial k}{\partial y}(x, y \to \mathit{fs}) &= \frac{\partial \varepsilon}{\partial y}(x, y \to \mathit{fs}) = 0
\end{aligned}
\tag{3.17}
$$

where $\mathit{fs}$ refers to the free-stream in boundary layers and the centerline coordinate in both channel and pipe flows.

## Numerical Solutions

The following sections will overview the results obtained with BASS for the solution of fully-developed turbulent channel flow and turbulent boundary layers.

### Turbulent Channel Flow

Like the laminar flow runs, for turbulent channel and boundary layer runs, nearly converged velocity profiles were used as the initial conditions. In the channel flow case, the profiles were already fully-developed and this allowed for the use of a very short grid. Like with the laminar flow grids, special attention was placed on the grid aspect ratios and an attempt at keeping the maximum value below the 1000 range was made. The grid shown in Figure 19 shows the turbulent channel geometry used with BASS and has a channel half-height of $0.0085m$ and a length of $0.05m$. It has a grid density of 201-by-
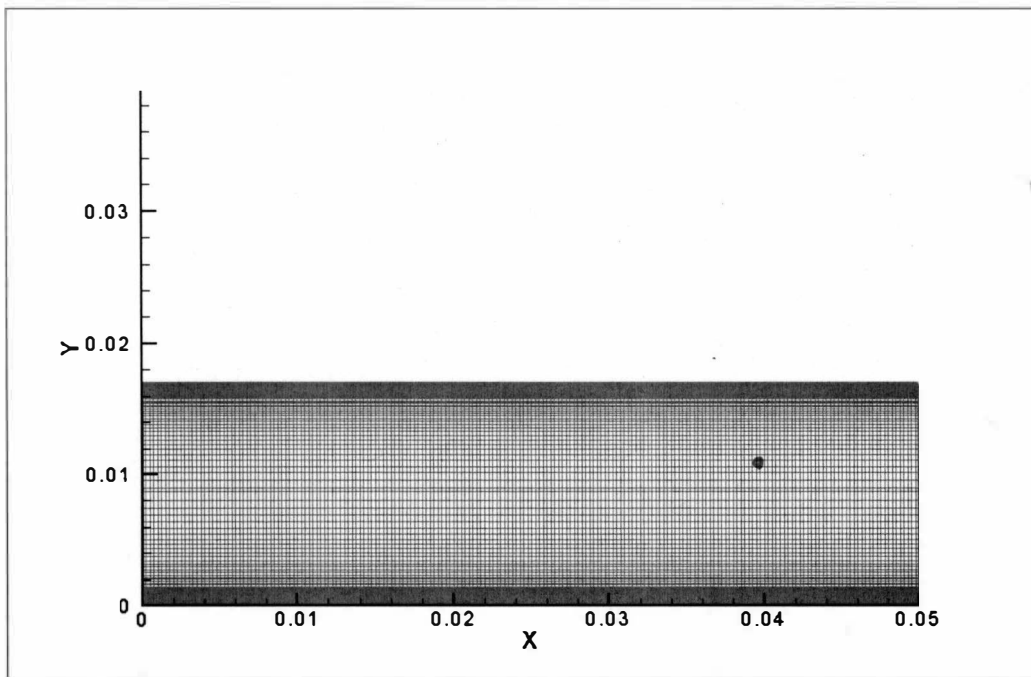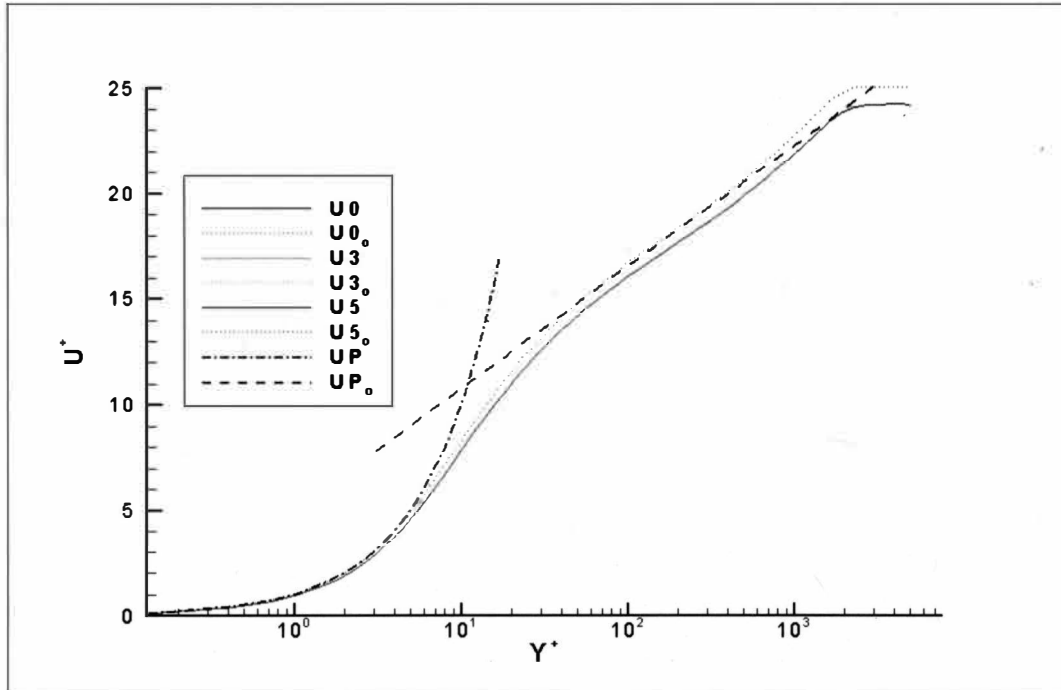
Figure 19. Turbulent Channel Grid.



Figure 20. Mean-Velocity Profiles at $\mathrm{Re}_\tau = 8{,}300$.

187 grid points. The reason for using so many points was to try and avoid any significant problems with the resolution of the scales near the walls.

The first test run with BASS was performed at a Reynolds number based on channel half-height and friction velocity, $u_\tau$, of 8,300. This is well within the domain of the flow being turbulent within the channel. To verify the numerical solution, plots for the wall-layer equations, Equations (3.10 and 3.11), were included. These correspond to the dark, dashed lines labeled as $UP$ and $UP_o$ in Figure 20. The dotted, colored lines correspond to the initial conditions used to start the numerical solution while the solid ones are the converged profiles obtained by BASS. As can be seen, the curves are presented in their nondimensional form of Equation (3.9).

In order to obtain additional information on whether or not the turbulence model in BASS is working, a simple mixing length model was also coded. A mixing length model can also be referred to as a zero-equation model since it does not solve any additional transport equations; its formulation for length and velocity scales are simply algebraic expressions. Figure 21, below, compares the same numerical velocity profile obtained with BASS and the turbulence model with the computational results from this last model. As can be seen, both are working properly and are resolving the appropriate dynamics close to the wall.

These results look promising. The kinetic energy profiles for the same run look good as well, suggesting that the model is working properly. These can be seen in Figure 22, below. The x-axis corresponds to the $Y^+$ values while $K^+ = {K_{(i,j)}}\big/{u_\tau^2}$ is assigned the y-axis. The subscripts $i,j$ are used to designate grid location.
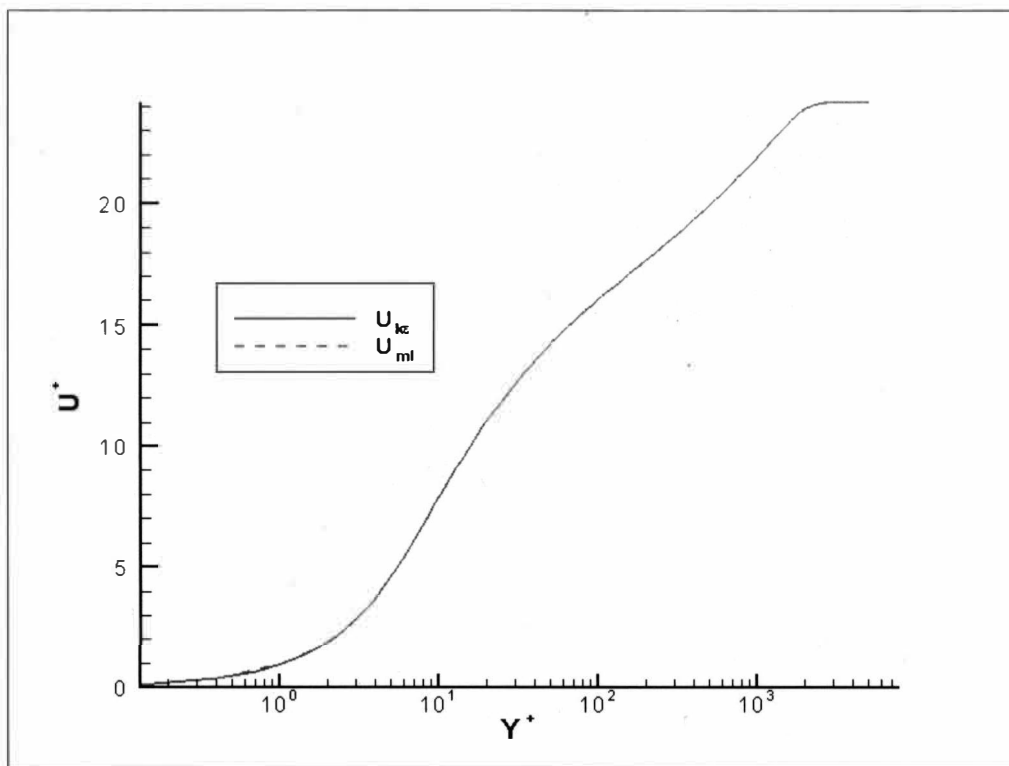
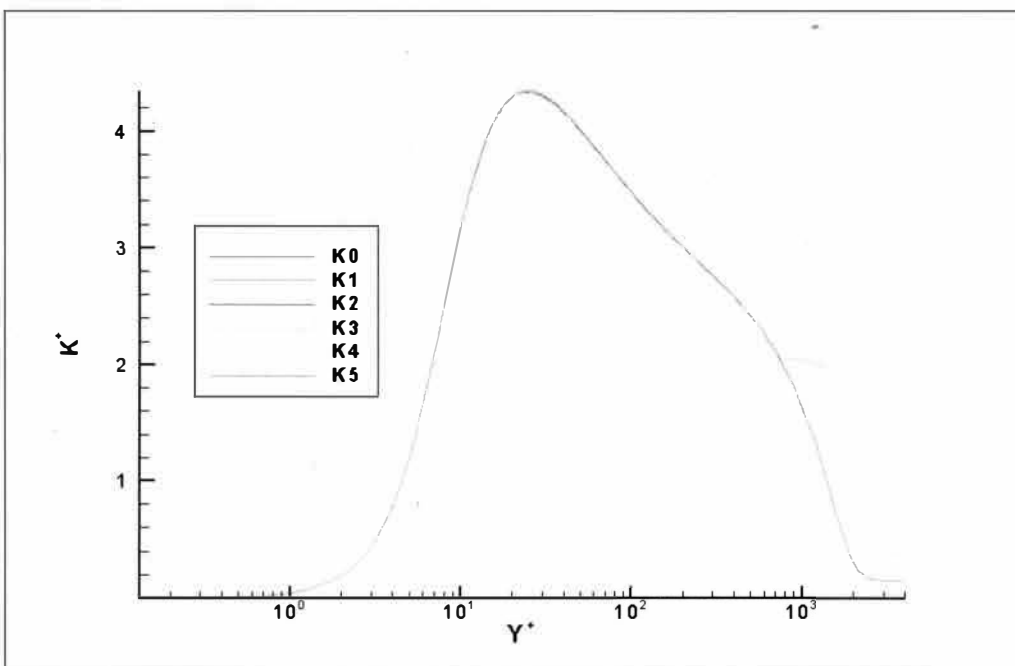Figure 21.  Comparison of Mean-Velocity Profiles for Both Turbulence Models.



Figure 22.  Mean-Kinetic Energy Profiles for $Re_\tau = 8,300$ Channel Flow.

53

## Turbulent Boundary Layer

Since turbulent channel flow is known to be relatively simple by nature, the real test of the code's prowess comes in the boundary layer computations. Chien's model has been shown to perform well in boundary layer flows, so the real test here is of BASS's numerical structure and, again, its viscous solving routines. The boundary layer grid is picture in Figure 23 and has a density of 101-by-150 points with the plate situated at $y=0$. Unlike the turbulent channel, this grid was purposefully extended in order to eliminate any uncertainty on whether or not the flow had fully-developed.

Data courtesy of Liou (2005) was utilized to startup the computations. The free-stream Mach number was set at 0.5. Figure 24 shows the mean-velocity profiles at Reynolds numbers based on momentum thickness, $\theta$, of 28,500 and 55,000. In the figure, the solid lines correspond to the data obtained with BASS's $k$-$\varepsilon$ model while the symbols represent Liou's data. Also, one additional curve per Reynolds number was plotted. These two curves correspond to the mixing length model previously introduced; they are represented in the curve by the dashed lines and can be seen to also agree well with both Liou's and BASS's data. Lastly, the curves named $UP_{log}$ and $UP$ correspond to the *Law of the Wall*, the same expressions as in Figure 17.

The kinetic energy ($k$) and energy dissipation ($\varepsilon$) profiles also provide a good measure of the current model's performance. Figures 25 and 26 show the excellent agreement between the initial and numerical data for these two key parameters. The curves are at the same Reynolds numbers as Figure 24. Since a mixing length model is a simple algebraic one, it does not solve for complicated parameters like the kinetic energy
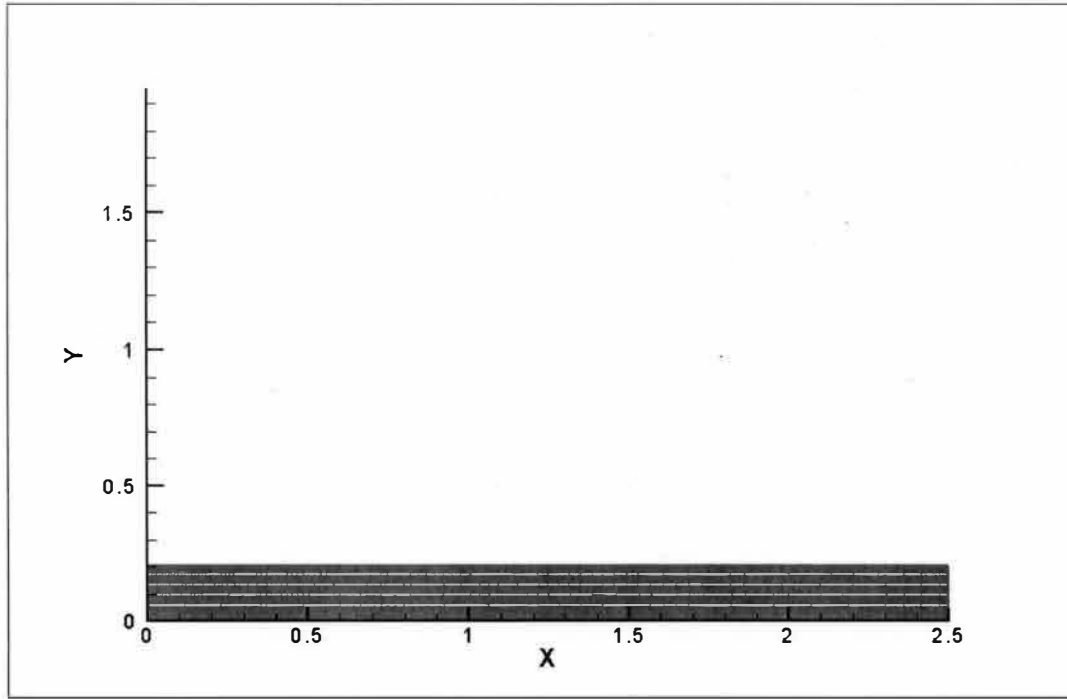
Figure 23. Turbulent Boundary Layer Grid.

or its dissipation. For this reason, curves for these parameters cannot be included.

Additionally, the kinetic energy is scaled to outer variable form, *ie* that of Figure 22,

along with its dissipation rate, which turns out to be $\varepsilon^+ = \dfrac{\varepsilon v}{u_\tau^4}$ .

For boundary layers, it is customary to include plots for a friction parameter, in

this case the local skin friction coefficient, $C_f$. To make a direct comparison, an

approximation for the skin friction based on the power law (Schlichting, 1979) was used,

$$C_f = \frac{0.074}{\mathrm{Re}_x^{1/5}} \tag{3.18}$$

This plot (Figure 27) shows the variations in skin friction for the two-equation model of

interest (solid line), the mixing length model for data verification (dashed line), Liou's

initial conditions (square symbols) and Schlichting's approximation (delta symbols). It
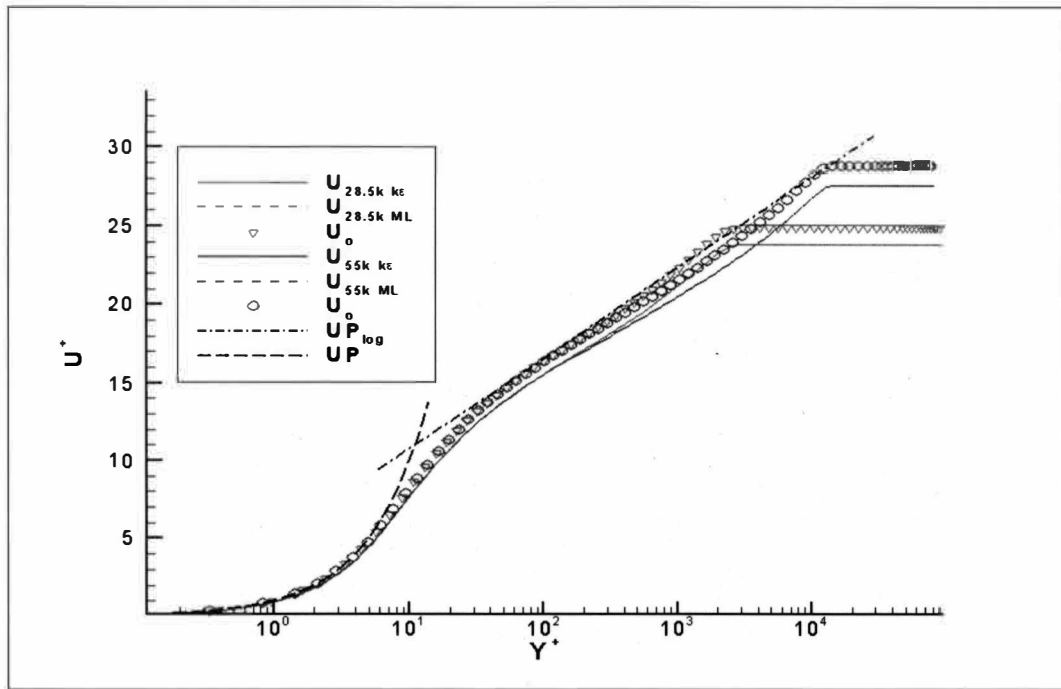
Figure 24.  Mean-Velocity Profiles for Turbulent Boundary Layer at $Re_\theta$ = 28,500 and 55,000.
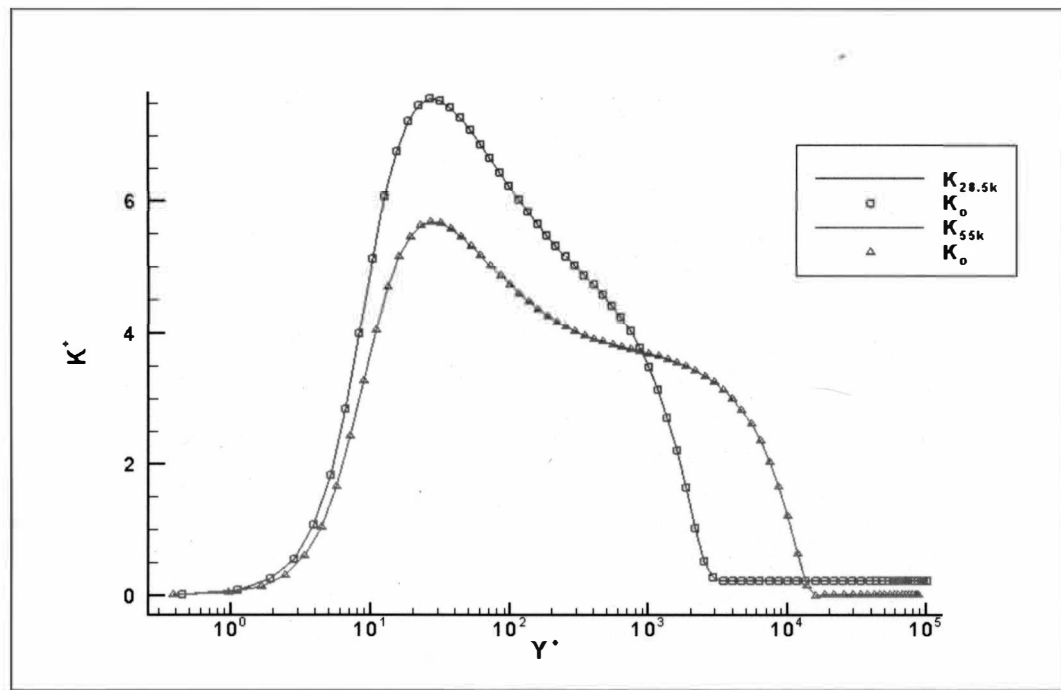


Figure 25.  Mean Kinetic Energy ($k$) Profiles at $Re_\theta$ = 28,500 and 55,000.

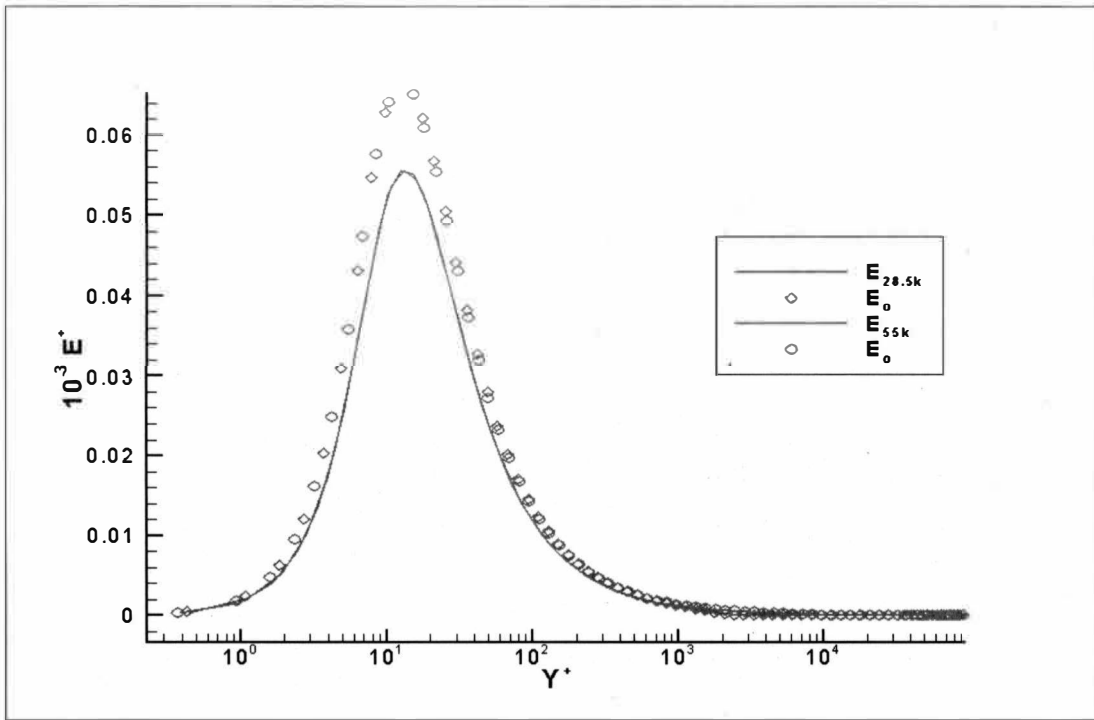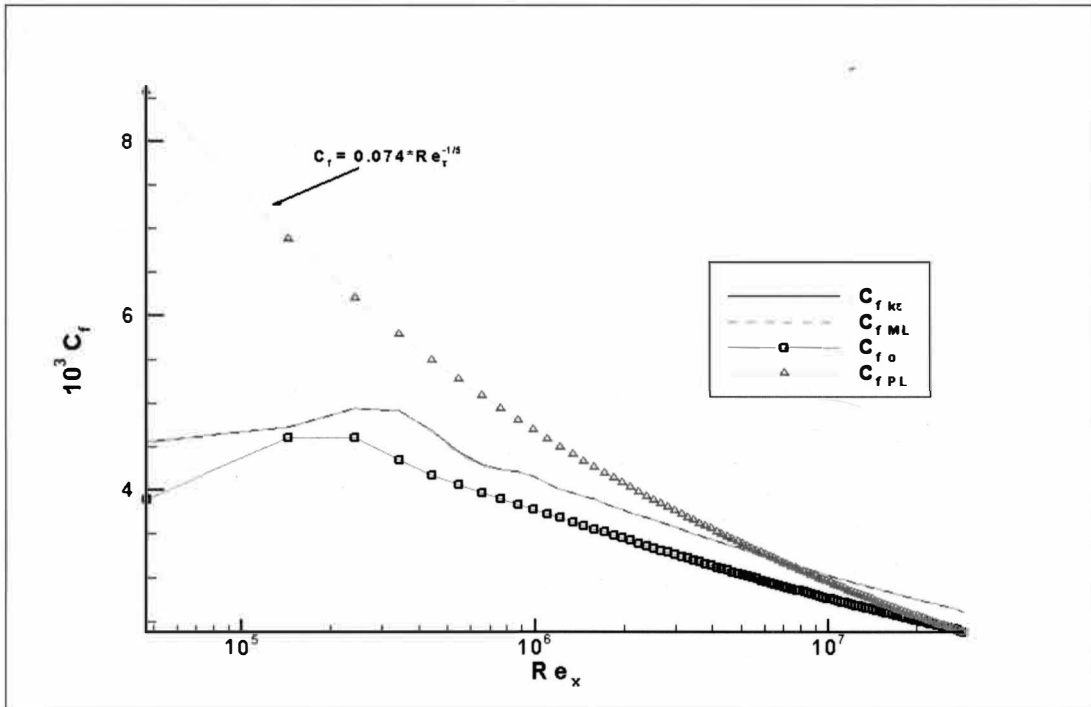Figure 26.  Dissipation of Energy ($\varepsilon$) Profiles at $Re_\theta = 28{,}500$ and $55{,}000$.



Figure 27.  Skin Friction Coefficient ($C_f$) Variation for Turbulent Flow over Flat Plate.

can be seen that, initially all of the numerical curves predict too small a skin friction whereas Liou's data approximates the empirical curve rather well at the higher Reynolds numbers. However, the data obtained with BASS does not deviate by more than around eight percent in the higher Reynolds number ranges.

One curve that was of particular interest was that of the variation of both laminar and turbulent viscosity parameters. This variation was split into two figures, one showing the ratio of turbulent-to-laminar viscosities (Figure 28) while the other showed the independent variations of each parameter across the boundary layer thickness (Figure 29). The data presented in these figures is for turbulent flow at a Reynolds number theta of 42,340.

As expected, Figure 29 confirms the notion that the area immediately adjacent to a wall is dominated by molecular viscosity. This is evident by the fact that in this small region, the molecular viscosity starts at its peak value, here roughly $4.28 \cdot 10^{-8}$, while the turbulent viscosity needs to develop until it overtakes the molecular effects. The rate at which the turbulent viscosity overtakes the laminar effects is astonishing; it quickly grows to be two orders of magnitude larger than the molecular viscosity. One final thing to note on these viscosities is that they are nondimensional; both are scaled by the reference Reynolds number, which is based on the speed of sound and a reference length of *1.0m*, as discussed in Chapter I.

The last order of business was verifying whether or not the solutions obtained and presented here are *grid independent*. Testing for grid independence is of use since it tells us how the code is reacting to refinements in the grid density. If the solution is truly grid
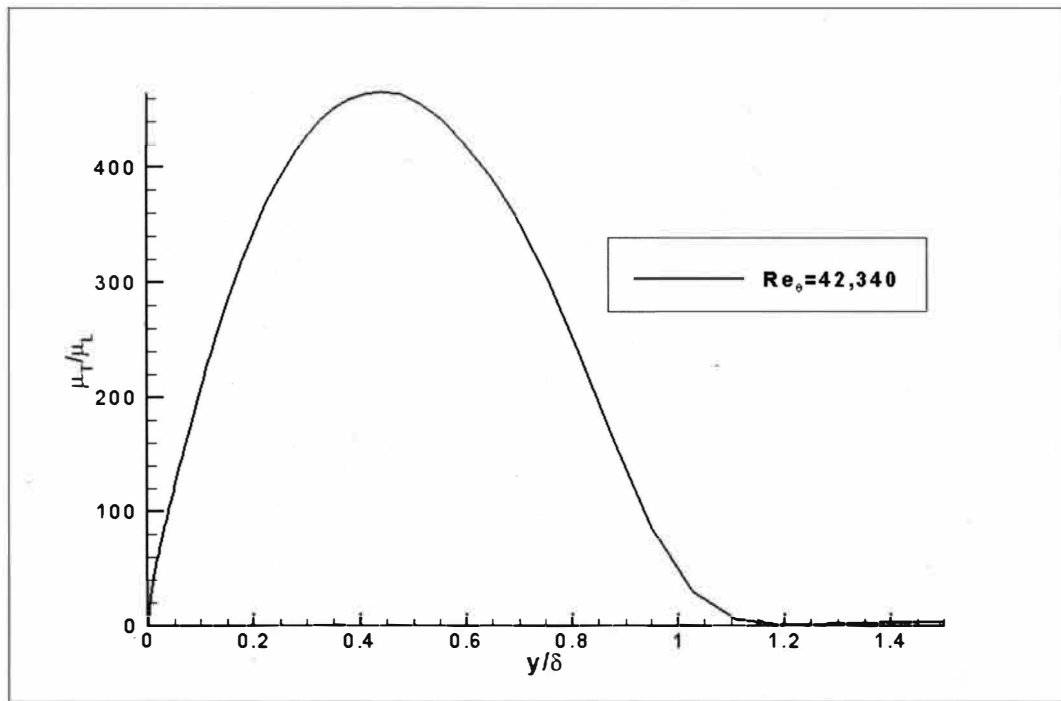
Figure 28.  Turbulent-to-Laminar Viscosity Ratio $\left(\mu_T/\mu_L\right)$ at $Re_\theta = 42{,}430$.
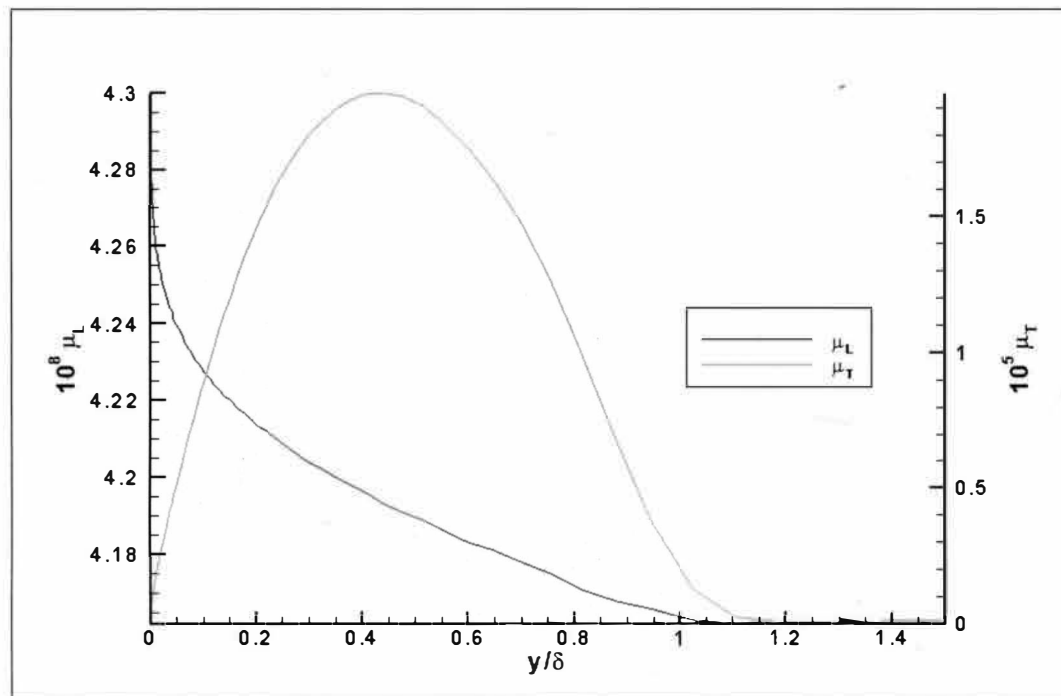


Figure 29.  Independent Variation of the Viscosities across the Boundary Layer.

independent, refinements in the grid will not translate to much variation in the converged results. Figure 30 shows tests performed on the boundary layer grids for this dependency. The grid densities used were 75, 101, or 150 points in the y-direction coupled with 101 points along the direction of the flow ($x$). The profiles used for comparison in the figure were those at a local Reynolds number of 28,500, as in Figure 24, which corresponds to the fine grid (*150* j-points). The profile from this latter figure is the red, solid line. The green-dashed and the blue, dashed-dotted lines are the results for the medium (*101*j-points) and the coarse (*75* j-points) grids, respectively. Even with a grid as coarse as 75 grid points in the y-direction gives very reasonable results and hence the solutions for these turbulent runs can be deemed grid independent.
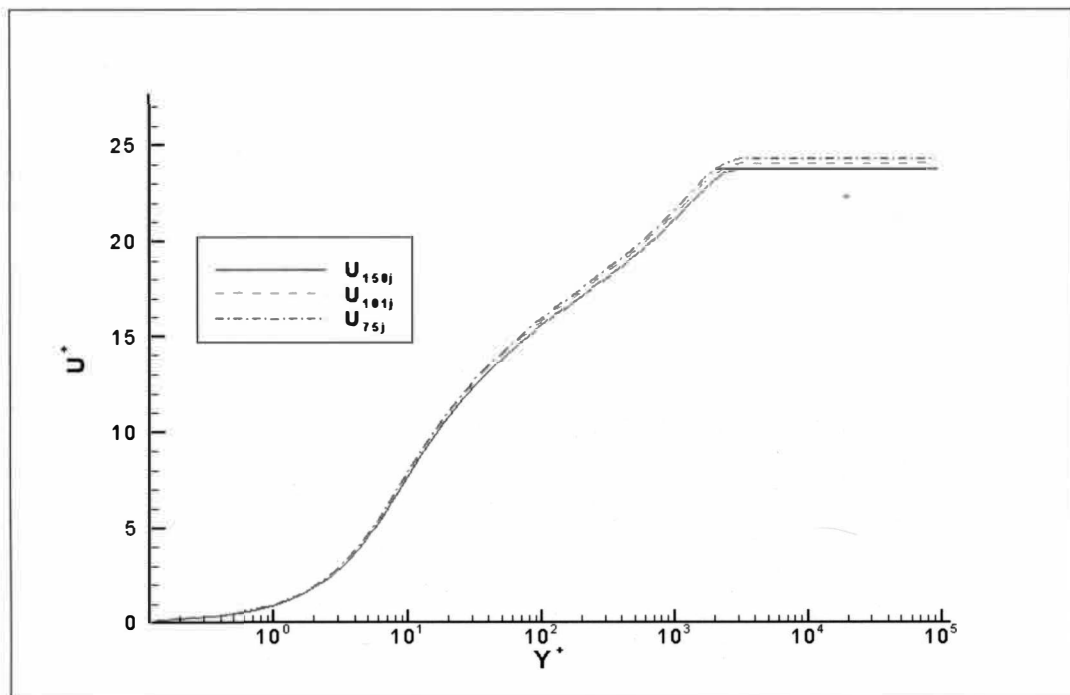


Figure 30. Grid Independence Comparison.

# Summary

The successful implementation of Chien's $k$-$\varepsilon$ model has been verified by the numerical computation of both turbulent channel and boundary layer flows. The data presented for both are promising in that they show BASS is now capable of handling turbulent flows at low turbulent Reynolds numbers. As was seen in the laminar flow runs, BASS tends to be extremely sensitive to initial and boundary conditions. This, again, forced us to develop realistic data to provide as the appropriate conditions.

# CHAPTER IV

## CONCLUSIONS

The verification of BASS's viscous solving routines has been verified by comparing numerical results to known analytical solutions to both channel and boundary layer flows. The results were promising. Because of the simplicity in flow dynamics in channels, agreement between the analytical results and those of BASS was excellent; for boundary layers, the data showed some variation from the analytical Blasius solution, but was never greater than a two percent difference in the laminar cases.

The addition of a low-Reynolds number two-equation turbulence model to BASS was also successful. Again, the model was tested in channel and boundary layer geometries and the results were good. All the appropriate dynamics in turbulent parameters, *ie* turbulent kinetic energy, dissipation of energy rates, and turbulent viscosities, were resolved adequately.

The following is future work that is suggested.

Even though the turbulence model has extended BASS's capabilities, the model still has its deficiencies. As discussed on Chapter III, the Chien model currently implemented has a direct dependency on the wall-normal Reynolds number parameter, $y^+$. Problems will therefore be encountered when using this model in flows with appreciable separation. This is because $y^+$ is indirectly proportional to the friction velocity, $u_\tau$, which becomes undefined in regions of separation causing a singularity in

the model prescription and rendering any numerical solution meaningless. Additionally, the model uses constants significantly different than the standard model, indicating that there may be differences between solutions obtained with the standard model and Chien's at high Reynolds numbers.

Because of this, it is desired to implement an additional variation of the $k-\varepsilon$ model to BASS. Now that it is certain the code is capable of handling viscous, turbulent flows and knowing it has the ability of analyzing complex flow geometries, it is of interest to implement Shih and Lumley's (1993) turbulence model. This model is of interest for several reasons. First, many experimenters have noted over the years the fact that model constants vary depending on flow complexity; this has been noted by Cazalbou, *et al* (1993) among others. To deal with this fact, Shih and Lumley proposed a model in which the constant $C_\mu$ is made dependent on the mean strain rate. It takes the following form,

$$C_\mu = \frac{1}{A_o + A_s U^{(*)} \dfrac{k}{\varepsilon}}$$

(4.1)

where the parameters $A_o$, $A_s$, and $U^{(*)}$ introduce the dependency of $C_\mu$ on the mean strain rate. The other model constants, $C_{\varepsilon 1}$, $C_{\varepsilon 2}$, and $Pr_\varepsilon$ are the same as in the high Reynolds number standard $k-\varepsilon$. This model has been extensively tested and has been seen to work very well for a range of flows (Liou *et al*, 2000).

The second reason the model is of interest is in the wall damping function of the turbulent viscosity, $f_\mu$. As stated earlier, Chien's model is dependent on $y^+$, and it comes into play in the turbulent viscosity and in the dissipation equation. To remove this dependency, Shih and Lumley, as well as Yang and Shih (1993) propose a wall damping

function that is a function of $R_y = \rho\sqrt{k}\,y/\nu$ instead of $y^+$. In doing so, the singularity encountered when a model is dependent on the friction velocity is completely eliminated, allowing the model to be applicable in separated flows.

With this model in place, it is the hope of the author to be able to simulate turbulent flows over more complicated geometries such as airfoils. This will make BASS of formidable code; being capable of resolving solutions fine enough for acoustics propagation while also being a useful tool for more commonplace computational fluid dynamics solutions.

# APPENDIX

## NOMENCLATURE

The following is the nomenclature for the parameters found in the equations published in the thesis:

### Governing Equation Variables:

| | | |
|---|---|---|
| $i,j$ | = | 1,2,3 |
| $x_i$ | = | three spatial coordinates |
| $t$ | = | time |
| $(\ )^*$ | = | nondimensional parameter |
| $\rho$ | = | density |
| $u_i$ | = | three velocity components |
| $E$ | = | total energy |
| $e$ | = | internal energy |
| $q$ | = | heat vector |
| $p$ | = | pressure |
| $p_o$ | = | initial pressure |
| $R$ | = | ideal gas constant |
| $T$ | = | temperature |
| $C_v$ | = | specific heat in constant volume |

$\delta_{ij}$ = Kronecker delta function ( 1 if $i=j$, 0 if $i \neq j$ )

$\tau_{ij}$ = laminar stress tensor

$\tau_w$ = wall shear stress

$G_i$ = body forces

$\mu(\mu_L)$ = dynamic viscosity

$\nu$ = kinematic viscosity

$k$ = thermal conductivity

$\gamma$ = ratio of specific heats *(= 1.4)*

$Pr$ = Prandtl number

$Re$ = Reynolds number

## Laminar Flow Runs:

$U_\infty$ = free-stream velocity

$\delta$ = boundary layer thickness

$\delta^*$ = boundary layer displacement thickness

$\Theta$ = boundary layer momentum thickness

$\eta$ = Blasius similarity variable

$C_f$ = skin friction coefficient

$R$ = residual

$N$ = total number of points

## Turbulent Governing Equations:

$u_\tau$ = friction velocity

$T_{ij}$ = subgrid-scale tensor

$\overline{S}_{ij}$ = mean strain-rate

$\mu_T$ = turbulent *(eddy)* viscosity

$\tau'_{ij}$ = turbulent stress tensor

$q'_i$ = turbulent heat vector

$\Phi'_{ij}$ = turbulent heat flux

$\widetilde{k}$ = turbulent kinetic energy

$\widetilde{\varepsilon}$ = dissipation rate of turbulent kinetic energy

$C_\mu$ = diffusion constant based on oscillating grid turbulence

$C_{\varepsilon 1}$ = model constant based on homogeneous shear flow

behind a grid

$C_{\varepsilon 2}$ = model constant based on isotropic grid turbulence data

$\left.\begin{array}{c} f_\mu \\ f_1 \\ f_2 \end{array}\right\}$ = wall-damping functions for $k$-$\varepsilon$ model

$\mathrm{Pr}_T$ = turbulent Prandtl number

$\kappa$ = von Karman constant

67

## Boundary Conditions:

$c_1, c_2, c_3, c_4$     = one-dimensional characteristic waves

$\bar{c}, a$     = speed of sound

## Outer Variable Nondimensional Variables:

$U^+$     = turbulent nondimensional velocity $\left( U^+ = U/u_\tau \right)$

$Y^+$     = wall-normal turbulent Reynolds number $\left( Y^+ = u_\tau y/\nu \right)$

$K^+$     = nondimensional turbulent kinetic energy $\left( K^+ = \tilde{k}/u_\tau^2 \right)$

$\varepsilon^+$     = nondimensional turbulent dissipation rate $\left( \varepsilon^+ = \varepsilon \nu/u_\tau^4 \right)$

# BIBLIOGRAPHY

Anderson, N., Eriksson, L.,-E., and Davidson, L. (2005). Large-eddy simulation of subsonic turbulent jets and their radiated sound. *AIAA Journal*, 43(9), 1899-1911.

Cazalbou, J. B. and Bradshaw, P. (1993). Turbulent transport in wall-bounded flows. Evaluation of model coefficients using direct numerical simulation. *Physics of Fluids A*, 5(12), 3233-3239.

Chen, C. -J. and Jaw, S. –Y. (1998). *Fundamentals of Turbulence Modeling*. Washington: Taylor and Francis.

Chien, K. –Y. (1982). Predictions of channel and boundary-layer flows with a low-Reynolds-number turbulence model. *AIAA Journal*, 20(1), 33-38.

Coakley, T. J. (1983). Turbulence modeling methods for the compressible Navier-Stokes equations. *AIAA Paper* 1983-1693.

Ghosal, H. and Moin, P. (1995). The Basic equations for the large eddy simulation of Turbulent flows in complex geometry. *Journal of Computational Physics*, 118, 24-37.

Giles, M. B. (1990). Nonreflecting boundary conditions for Euler equation calculation. *AIAA Journal*, 28(12), 2050-2058.

Harlow, F. H. and Nakayama, P. I. (1968). Transport of Turbulence Energy Decay Rate. *Los Alamos Scientific Laboratory Report* LA-3854. Los Alamos, New Mexico.

Henkes, R. A. W. M. (1998). *Overview of Turbulence Models for External Aerodynamics*. Netherlands: Delft University Press.

Hinze, J. O. (1975). *Turbulence*. New York: McGraw-Hill, Inc.

Hixon, R., Shih, S. –H. and Mankbadi, R. R. (1995). Evalation of boundary conditions for computational aeroacoustics. *AIAA Journal*, 33(11), 2006-2012.

Hixon, R. (1997). Evaluation of a high-accuracy MacCormack-type scheme using benchmark problems. NASA Contractor Report 202324.

Hixon, R. and Turkel, E. (2000). Compact implicit MacCormack-type schemes with high accuracy. *Journal of Computational Physics*, 158, 51-70.

Hixon, R., Shih, S. –H. and Mankbadi, R. R. (2000). Evaluation of boundary conditions for the gust-cascade problem. *Journal of Propulsion and Power*, 16(1), 72-78.

Hixon, R. (2000). Prefactored small-stencil compact schemes. *Journal of Computational Physics*, 165, 522-541.

Hu, F. Q., Hussaini, M. Y., and Manthey, J. (1996). Low-dissipation and low-dispersion Runge-Kutta schemes for computational acoustics. *Journal of Computational Physics*, 124, 177-191.

Jones, W. P. and Launder, B. E. (1972). The Prediction of laminarization with a two-equation model of turbulence. *International Journal of Heat and Mass Transfer*, 15, 301-314.

Jones, W. P. and Launder, B. E. (1973). The Calculation of low-Reynolds-number phenomenon with a two-equation model of turbulence. *International Journal of Heat and Mass Transfer*, 16, 1119-1130.

Kim, J., Moin, P. and Moser, R. (1987). Turbulence Statistics in Fully Developed Channel Flow at Low Reynolds Number. *Journal of Fluid Mechanics*, 177, 133-166.

Kraichnan, R. H. (1976). Eddy viscosity in two and three dimensions. *Journal of the Atmospheric Sciences*, 33, 1521,1536.

Launder, B. E. and Spalding, D. B. (1972). *Lectures in Mathematical Models of Turbulence*. New York: Academic Press.

Layton, W. J. (2002). A mathematical introduction to large eddy simulation. *University Of Pittsburgh Technical-Report MATH 03-03*.

Lesieur, M. and Metais, O. (1996). New trends in large-eddy simulations of turbulence. *Annual Review of Fluid Mechanics*, 28, 45-82.

Liou,W. W. (2005). Private Communication.

Liou, W. W., Huang, G. and Shih, T. –H. (2000). Turbulence model assessment for shock wave/turbulent boundary-layer interaction in transonic and supersonic flows. *Computers and Fluids*, 29, 275-299.

Menter, F. R. (1994). Two-equation eddy-viscosity turbulence models for engineering Applications. *AIAA Journal*, 32(8), 1598-1605.

Munson, B. R., Young, D. F. and Okiishi, T. H. (1998). *Fundamentals of Fluid Mechanics*. New York: John Wiley and Sons.

Panton, R. L. (1996). *Incompressible Flow.* New York: John Wiley and Sons.

Reynolds, A. J. (1974). *Turbulent Flows in Engineering*. New York: John Wiley and Sons.

Schlichting, H. (1979). *Boundary-Layer Theory*. New York: McGraw-Hill, Inc.

Sherman, F. (1990). *Viscous Flow*. New York: McGraw-Hill Publishing Company.

Shih, T. –H., Liou, W. W., Shabbir, A., Yang, Z. and Zhu, J. (1994). A New $k$-$\varepsilon$ viscosity model for high Reynolds-number turbulent flows. *Computers and Fluids*, 24(3), 227-238.

Shih, T. –H., Zhu, J., and Lumley, J. L. (1994a). A new Reynolds stress algebraic equation model. NASA TM 106644.

Shih, T. –H. and Lumley, J. L. (1993). Kolmogorov behavior of near-wall turbulence and its application in turbulence modeling. *Computational Fluid Dynamics*, 1, 43-56.

Smagorinsky, J. (1963). General circulation experiments with the primitive equations. *Monthly Weather Review*, 91(3), 99-164.

Stanescu, D. and Habashi, W. G. (1998). *2N*-Storage low dissipation and dispersion Runge-Kutta schemes for computational aeroacoustics. *Journal of Computational Physics*, 143, 674-681.

Tam, C. W. and Dong, T. Z. (1994). Wall boundary conditions for high-order finite-Difference schemes in computational aeroacoustics. *Theoretical Computational Fluid Dynamics*, 6(5-6), 303-322.

Tam, C. K. W. and Webb, J. C. (1993). Dispersion-relation-preserving finite difference Schemes for computational acoustics. *Journal of Computational Physics*, 107, 262-281.

Tam, C. K. (1995). Computational aeroacoustics: issues and methods. *AIAA Journal*, 33(10), 1788-1796.

Tannehill, J. C., Anderson, D. A. and Pletcher, R. H. (1997). *Computatinal Fluid Mechanics and Heat Transfer*. Philadelphia: Taylor and Francis.

Tennekes, H. and Lumley, J. L. (1972). *A First Course in Turbulence*. Cambridge: The MIT Press.

Thompson, K. W. (1987). Time-dependent boundary conditions for hyperbolic systems. *Journal of Computational Physics*, 68(1), 1-24.

Thompson, K. W. (1990). Time-dependent boundary conditions for hyperbolic systems. *Journal of Computational Physics*, 89(2), 439-461.

Wilcox, D. C. (1998). *Turbulence Modeling for CFD*. La Canada: DCW Industries.

Yang, Z. and Shih, T. –H. (1993). New time scale based $k$-$\varepsilon$ model for near-wall Turbulence. *AIAA Journal*, 31(7), 1191-1198.